Stability and Control CFD Investigations of a Generic 53° Swept UCAV Configuration

Neal T. Frink[1]
NASA Langley Research Center, Hampton, Virginia 23681, USA

NATO STO Task Group AVT-201 on "Extended Assessment of Reliable Stability & Control Prediction Methods for NATO Air Vehicles" is studying various computational approaches to predict stability and control parameters for aircraft undergoing non-linear flight conditions. This paper contributes an assessment through correlations with wind tunnel data for the state of aerodynamic predictive capability of time-accurate RANS methodology on the group's focus configuration, a 53° swept and twisted lambda wing UCAV, undergoing a variety of roll, pitch, and yaw motions. The vehicle aerodynamics is dominated by the complex non-linear physics of round leading-edge vortex flow separation. Correlations with experimental data are made for static longitudinal/lateral sweeps, and at varying frequencies of prescribed roll/pitch/yaw sinusoidal motion for the vehicle operating with and without control surfaces. The data and the derived understanding should prove useful to the AVT-201 team and other researchers who are developing techniques for augmenting flight simulation models from low-speed CFD predictions of aircraft traversing non-linear regions of a flight envelope.

Nomenclature

b	=	wing span, =1.538m
b_{ref}	=	reference span (b/2), =0.769m
C_L	=	lift coefficient, =Lift/$q_\infty S_{ref}$
C_{MX}	=	rolling moment coefficient about x-body axis, =Rolling_Moment/$q_\infty S_{ref} b_{ref}$
C_{MY}	=	pitching moment coefficient about y-body axis, =Pitching_Moment/$q_\infty S_{ref} c_{ref}$
C_{MZ}	=	yawing moment coefficient about z-body axis, =Yawing_Moment/$q_\infty S_{ref} b_{ref}$
C_N	=	normal force coefficient, =Normal_Force/$q_\infty S_{ref}$
C_p	=	pressure coefficient
c_r	=	wing root chord, =1.061m
c_{ref}	=	reference chord, =0.479m
f	=	sinusoidal oscillation frequency about pitch, roll, or yaw axis, Hz.
k_P	=	reduced frequency for pitch oscillation, $=2\pi f \cdot c_{ref}/U_\infty$
k_R, k_Y	=	reduced frequency for roll and yaw oscillation, $=2\pi f \cdot (b/2)/U_\infty$
LOB/LIB	=	left-outboard/left-inboard trailing-edge control surface deflections, positive downward
log(r/r0)	=	order of magnitude drop in solution residual, e.g. -4 means 4 orders of magnitude drop
M_∞	=	freestream Mach number
MRP	=	Moment Reference Point for pitching moment, =0.600m from apex
N_{cyc}	=	Number of time steps per oscillation cycle, $=2\pi/(k \bullet \Delta t^*)$
q_∞	=	Dynamic pressure, N/m^2
Re_{cref}	=	Reynolds number based on c_{ref}
ROB/RIB	=	right-outboard/right-inboard trailing-edge control surface deflections, positive downward
RRP	=	DNW-NWB rear rotation point for pitch and yaw oscillation, =0.855m from apex
rate1 & rate2	=	primary& secondary VGRID "viscous" stretching factors, see Eq. 1
S_{ref}	=	reference area, =0.77m^2
Δt	=	physical time step, seconds
Δt^*	=	characteristic time step, $=\Delta t \bullet U_\infty / c_{ref}$

[1] Senior Researcher, Configuration Aerodynamics Branch, Research Directorate, MS 499, Associate Fellow, AIAA

U_∞ = freestream velocity, ≈50m/s
α = angle of attack, deg.
β = angle of sideslip, deg. Positive nose left (wind from right).
δ_{i+1} = VGRID "viscous" grid spacing normal to surface at node $i+1$, see Eq. 1, meter
δ_1 = spacing of first node off of surface in "viscous" grid layers, see Eq. 1, meter
Φ_0 = nominal roll angle, deg.
$\Delta\Phi$ = range of roll oscillation about Φ_0 through body axis, +/-deg.
Θ_0 = nominal pitch angle, deg.
$\Delta\Theta$ = range of pitch oscillation about Θ_0 through body axis, +/-deg.
Ψ_0 = nominal yaw angle, deg.
$\Delta\Psi$ = range of yaw oscillation about Ψ_0 through body axis, +/-deg.

Key Acronyms
AVT = Applied Vehicle Technology
CFD = Computational Fluid Dynamics
CS0 = DLR-F19 with undeflected control surfaces
CS20 = DLR-F19 with deflected control surfaces, LOB/LIB=-20/-20, ROB/RIB=+20/+20 deg
DOF = Degree-of-freedom
DNW-NWB = German-Dutch Wind Tunnel located in Braunschweig
F-O = Forced-oscillation sinusoidal motion
KE, k-ε = Jones-Launder linear k-epsilon two equation turbulence model
NATO/STO = North Atlantic Treaty Organization / Science and Technology Organization
RANS = Reynolds Averaged Navier Stokes
SA = Spalart-Allmaras one equation turbulence model
SID = System identification
SST = Menter's Shear Stress Transport two equation turbulence model
UCAV = Unmanned Combat Air Vehicle

I. Introduction

Historically, many civil and military aircraft development programs have encountered costly stability and control (S&C) deficiencies during early stages of flight test despite thousands of hours of wind tunnel testing. These surprises have occurred across the speed range from takeoff and landing to cruise flight, and particularly at the fringes of the flight envelope where separated flows dominate. It is widely believed within the research community that the next significant advancement in the state of the art for predicting the S&C characteristics of a new vehicle might be through the application of computational fluid dynamics (CFD) tools. The application of high-end CFD codes with Reynolds-averaged Navier Stokes (RANS) or better level of technology to specific areas of S&C interest before first flight can help focus wind tunnel programs and provide improved understanding of the underlying flow physics. A focus for such an advancement has been fostered by a coordinated international team of researchers under the NATO/STO AVT-161 Task Group titled "Assessment of Stability and Control Prediction Methods for NATO Air & Sea Vehicles" (2007-2010) [1] and the AVT-201 Task Group titled "Extended Assessment of Reliable Stability & Control Prediction Methods for NATO Air Vehicles" (2011-2015) [2]. Under AVT-201, the focus has been extended to include investigation of applying system identification (SID) techniques to CFD-derived S&C data for constructing reduced-order models for flight simulators. NASA is also leveraging this NATO activity to guide a parallel study of S&C CFD modeling and SID for civil transports near stall within the Vehicle Systems Safety Technology project under the NASA Aviation Safety Program [3].

The prevalent experimental methodology for quantifying the dynamic stability of an aircraft calls for extracting the dynamic stability derivatives from the force and moment coefficients as the aircraft undergoes a periodic motion about a body axis in a wind tunnel. Experimentalists within the AVT-161 and AVT-201 teams have conducted dynamic wind-tunnel tests on the focus configuration, called **S**tability **a**nd **C**ontrol **Con**figuration (SACCON), undergoing pitch, roll, and yaw oscillation to measure the dynamic stability and aerodynamic characteristics [4,5]. Other team members are running parallel dynamic computational studies following a similar approach of modeling SACCON undergoing pitch, roll, and yaw oscillation with their respective CFD tools [6-12]. Alternative approaches applying system identification techniques to multiple frequency/amplitude motions [13], and more recently exploring indicial maneuvers [14] that have the potential of reducing the computational cost for constructing dynamic derivatives by a factor of five. The collective experiences from these studies have confirmed the difficulty

of achieving accurate and efficient computation of dynamic stability characteristics for the highly nonlinear portions of the flight envelope.

For purposes of coordinating a focused international research study, the AVT-201 Task Group defined a set of common static and dynamic SACCON test cases for team members to compute [15]. These cases include static angle of attack (alpha) and sideslip (beta) sweeps and select dynamic forced-oscillations about the pitch and yaw axes for various combinations of control surface deflections. This paper documents a NASA CFD investigation of SACCON S&C characteristics for subset of the AVT-201 common test cases. The roll oscillation solutions are computed for an AVT-161 test case without control surface deflections. A limited static study is performed to gain understanding of grid and turbulence model sensitivities, which will provided guidance for dynamic force-oscillation computations that follow.

II. Geometry and Experiment

A. General description and reference conditions

The SACCON geometry presented in Fig. 1 is a generic representation of a UCAV configuration with 53-deg swept leading-edge. The variation used in this investigation has a sharp inboard leading edge segment that transitions to a "medium" round leading edge on the outer wing panel. This outer panel has parallel leading and trailing edges that twist 5-deg in washout. As noted in Fig. 1, the wingspan is 1.54m, root chord is approximately 1m, and reference chord, c_{ref} is 0.48m. The reference area, S_{ref} is 0.77m^2. For pitch and yaw forced oscillation testing, the rear rotation point (*RRP*) is positioned near the aft end of the root chord, downstream of the aerodynamic moment reference point, *MRP*. With roll oscillation testing, the model rotates around an aft-mounted sting through the longitudinal axis.

Two SACCON wind tunnel models were used to provide correlation data for this study; the DLR-F17 used as the primary test article in the prior AVT-161 task group, and a new model with control surfaces designated DLR-F19. Both were constructed with the dimensions noted in Fig. 1 from lightweight composite material to facilitate dynamic oscillation testing. Both were equipped with pressure taps on the upper and lower surfaces of the model that are configured for dynamic measurement of unsteady pressures.

Initial tests with the DLR-F17 SACCON configuration during AVT-161 revealed an arbitrary boundary layer transition line on the upper surface of the model detected by infrared thermography. This discovery led to a decision to apply carborundum trip grit to fix transition near the leading edge. Transition of the boundary layer to fully turbulent flow was subsequently verified with this configuration mounted on a belly sting [4].

B. DLR-F19 SACCON with belly sting

The DLR-F19 wind-tunnel model was mounted to a six-component balance by a post sting attached to the underside at the RRP. The model is shown in Fig. 2 (left) mounted inverted in the closed test section of the German-Dutch Wind Tunnel (DNW-NWB) located in Braunschweig, Germany with the control surfaces deflected in the LOB/LIB=-20/-20, ROB/RIB=+20/+20 deg configuration. The location of the pressure rows on the DLR-F19 is shown in Fig. 1. A yaw-link support sting with 15^o crank angle was used for the static data and yaw oscillation cases. The pitch oscillation runs utilized a pitch-link support sting with 6^o crank angle and a 7th axis push rod. Forced motion was induced using the DNW-NWB Model Positioning Mechanism (MPM) that is a six degree-of-freedom (DOF) parallel kinematics system designed for static as well as for dynamic model support. The MPM is located above the test section and can be operated in the open test section as well as in the closed one. The location of oscillation axes can be chosen arbitrarily and in addition to classic sinusoidal oscillations the MPM can perform multi-DOF maneuvers. Details of the model, MPM, and the installation are described in Ref. [4].

In future references to the DLR-F19 configuration in this paper, the cases with undeflected control surfaces will be designated CS0. The cases with deflected control surfaces LOB/LIB=-20/-20, ROB/RIB=+20/+20 deg will be referenced as CS20.

C. DLR-F17 SACCON with aft sting

The DLR-F17 wind-tunnel model is shown in Fig. 2 (right) supported by an aft sting mount in the NASA Langley Research Center (LaRC) 14- by 22-Foot (4.3- by 6.7-meter) Subsonic Tunnel in Hampton, Virginia, United States. Forced sinusoidal motion was applied about the roll axis from a motor on the sting support system. The DLR-F17 was the primary SACCON test article in the AVT-161 task group. Hence, extensive force and moment, pressure, and Particle Image Velocimetry (PIV) flow measurement static and dynamic data is available for this configuration mounted on both belly sting and aft sting [4,5]. The surface of the model was painted with shiny black

paint that contains particles of Rhodamine B to reflect laser light at a different wavelength, which can be filtered so as to produce highly accurate PIV measurements close to the surface.

III. Methodology

The CFD computations are performed using the NASA Tetrahedral Unstructured Software System (TetrUSS) [16]. This system consists of loosely integrated, user-friendly software that comprises a geometry setup utility GridTool, a tetrahedral grid generator VGRID, a flow solver USM3D, and post-processing visualization and data extraction utilities. Body motion is controlled through a third-party process control framework called FD-CADRE.

A. Grid generator

VGRID [17,18] is a tetrahedral grid generator based on the advancing front method (AFM) for generation of surface triangles and "inviscid" field cells, and the advancing layers method (ALM) for generation of thin-layered "viscous" cells. Both techniques are based on marching processes in which tetrahedral cells grow from an initial front (triangular surface mesh) until the volume around the geometry is filled. Unlike the conventional AFM, which introduces cells into the field in a totally unstructured manner, the ALM generates organized layers of thin tetrahedral cells, one layer at a time, while maintaining the flexibility of AFM. Once the advancing front process is completed in VGRID, an additional postprocessing step is required using POSTGRID to close any open pockets and to improve grid quality. VGRID input files are generated by an interactive geometry manipulation program, GridTool. This graphics tool can import surface definitions from initial graphics exchange specification (IGES) files containing nonuniform rational B-spline surfaces and curves, as well as PLOT3D point definition files. GridTool is used to manipulate the geometry and to define necessary geometric surface patches and grid spacing (source) parameters.

B. Flow solver

The computations are performed with USM3D [19], which is a parallelized tetrahedral cell-centered, finite volume Navier-Stokes flow solver. The term "cell centered" means that the finite volume flow solution is solved at the centroid of each tetrahedral cell. Inviscid flux quantities are computed across each tetrahedral cell face using various upwind schemes. Spatial discretization is accomplished by a novel reconstruction process, based on an analytical formulation for computing solution gradients within tetrahedral cells. The solution can be advanced in time by a 2^{nd}-order "physical" time step scheme, a 2^{nd}-order "dual" time step scheme, or to a steady-state condition by an implicit backward-Euler scheme. Several turbulence models are available: the Spalart-Allmaras (SA) one-equation model, the two-equation k-ε turbulence model, the Menter Shear Stress Transport (SST) two-equation model, and the nonlinear Algebraic Reynolds Stress Models of Girimaji and Shih/Zhu/Lumley. Detached Eddy Simulation (DES) has been implemented in all of the turbulence models, but has not been fully tested. The latest extensions to the USM3D flow solver are described in Ref. [20].

C. General motion controller

The USM3D flow solver has been installed as a plug-in to the FD-CADRE framework (Fluid Dynamics – Computational Analysis of Dynamically Responsive Environments) [21] developed at Arnold Engineering Development Center in Tullahoma, Tennessee. FD-CADRE is a generalized dynamic process control manager for coupling various plugins, e.g. flow solver, 6-DOF motion generator, aeroelastic structural module, etc. The advantage is that one can couple an existing legacy code such as USM3D to additional tools that dramatically expand its analysis capabilities. The USM3D/FD-CADRE combination has been used heavily by users in the Department of Defense for computing complex moving-body problems with overset tetrahedral grids. The current work only utilizes the prescribed motion capability on non-deforming, non-overset grids.

D. Solution strategy

USM3D solutions are generated using an implicit second-order physical time-step scheme for both the static and dynamic cases. Inviscid fluxes are computed with Roe's flux difference scheme without limiting. The time-accurate RANS flow solutions are primarily computed with the SA turbulence model. Limited assessments are also made for the static cases with the SST and k-ε turbulence models. The boundary conditions consist of a surface no-slip constraint on the wing and support sting and characteristic inflow/outflow on the outer box. The forced oscillation (F-O) solutions are generated using nondeforming solid-body rotation of the full grid about the x, y, or z axis and initialized by restarting from a converged static solution at the prescribed angle of attack, α_0, and cycled for two full sinusoidal oscillations. However, the hysteresis of forces and moments is converged to its periodic solution after the

first quarter cycle of oscillation; only the second cycle is plotted in the correlation with experiment. Details of specific time step and turbulence model strategies will be included in Section VI.

IV. Grid Generation

A series of full-span tetrahedral grids were generated for the DLR-F19/F17 SACCON configurations shown in Fig. 3 using a developmental version of VGRID [18] and following guidelines developed in Ref. [6]. Thin-layer tetrahedral grids were generated to meet requirements for cell-centered computations from the USM3D flow solver. A near-wall first-cell spacing was prescribed, based on flat-plate turbulent boundary layer theory, to achieve a tetrahedral cell centroid turbulent wall coordinate (y^+) of *0.5* at a longitudinal distance of 0.5*c_{ref} for a Re_{cref}=1.5 million. Since the VGRID Advancing Layers Method marches nodes away from the vertices of the surface triangles (which are subsequently connected to form tetrahedral cells), an initial VGRID spacing, δ_1, corresponding to a $y^+=2$ at the first node was prescribed in order to achieve the $y^+=0.5$ at the first cell centroid. Subsequent USM3D computations confirmed that an average first-cell $y^+\approx0.4$ was achieved. For the SACCON at the nominal wind tunnel chord Reynolds number of 1.5 million, the required VGRID first-node spacing is $\delta_1/c_{ref}=2.4E\text{-}05$, and stretching factors of *rate1=0.15* and *rate2=0.02*, where the nodal spacing layers are defined by the Eq. (1).

$$\delta_{i+1} = \delta_1 \cdot [1 + rate1 \cdot (1 + rate2)^i]^i \tag{1}$$

The same "viscous" spacing distribution was applied to all DLR-F19 and DLR-F17 grids and resulted in approximately 72 tetrahedral cells (24 nodes) across the boundary layer at the mid-chord of c_{ref}.

Six grids were generated on the DLR-F19 configuration with the 15° yaw-link post sting; coarse/medium/fine (G1/G2/G3) with and without flap deflections with the characteristics listed in Table 1. Similarly, coarse/medium/fine grids were generated on the DLR-F17 with aft roll sting producing the characteristics listed in Table 2. In both cases, the VGRID sources from the grids in Ref. [6] were transferred into the VGRID input files for the current configurations, thereby insuring a consistency with the prior study.

Table 1 - General full-span mesh properties for DLR-F19 with 15° yaw-link belly sting.

Grid	*LOB/LIB* [°]	*ROB/RIB* [°]	*VGRID ifact*	*Tets* [millions]	*Nodes* [millions]	*Wing triangles*	*Wing nodes*
G1.00	-	-	1.9440	7.233	1.228	73,456	36,738
G2.00	-	-	1.4215	12.967	2.203	132,474	66,251
G3.00	-	-	1.0000	25.776	4.383	261,050	130,543
G1.20	-20/-20	+20/+20	1.9440	10.286	1.749	120,364	60,192
G2.20	-20/-20	+20/+20	1.4215	17.963	3.056	212,456	106,242
G3.20	-20/-20	+20/+20	1.0000	34.960	5.952	414,984	207,510

Table 2 - General full-span mesh properties for DLR-F17 with aft-roll sting.

Grid	*VGRID ifact*	*Tets* [millions]	*Nodes* [millions]	*Wing triangles*	*Wing nodes*
G1a	1.9440	6.523	1.228	71,706	35,881
G2a	1.4215	11.689	1.987	130,048	65,059
G3a	1.0000	23.185	3.943	256,664	128,379

The upper surface grid triangulations for G1.20, G2.20, and G3.20 are shown in Fig. 4 for the DLR-F19 with deflected control surfaces (CS20), along with corresponding volume grids slices through the right-wing control surface in Fig. 5. The grid refinement was achieved by changing the "*ifact*" parameter in the VGRID input, which globally scales the spacing for the "inviscid" portion of the grid, as highlighted in Fig. 5. The normal distributions across the "viscous" layers were not scaled in the process. Spanwise grid stretching with a ratio as high as 10-to-1 was applied along the leading- and trailing-edges for each G1, G2, and G3 as described in Ref. [6] in order to reduce cell count. Additional detail of the surface and volume grids in vicinity of the outboard gap for the right-wing control surface is provided in Figs. 6 and 7. The gap between abutting flap/wing surfaces was sealed.

V. Scope of Investigation

For the AVT-201 effort described in the Introduction, the task group developed a set of common test cases for the DLR-F19 SACCON configuration to be analyzed and compared amongst the team. These included both static alpha and beta sweeps, and some cases for dynamic forced oscillation about pitch and yaw axis, all with various combinations of control surface deflection [15]. A subset of the static α- and β-sweeps will be used to assess sensitivities of the flow solution to grid density and turbulence models. The static results then provided guidance for pursuing the dynamic cases. The roll oscillation study is performed on the DLR-F17 SACCON for correlation with NASA Langley Research Center 14X22 subsonic wind tunnel data obtained by the AVT-161 task group.

A. Static α and β sweeps

As depicted in Table 3, the static investigation includes two angle-of-attack sweeps from α=*0-30* deg, one with and one without control surface deflection. Solutions are provided at α= 0.0, 5.3, 10.0, 12.5, 14.7, 15.7, 16.8, 17.8, 18.9, 19.9, 22.5, 25.0, 30.0 deg and zero sideslip. Static sideslip sweeps of β=*+/-10* deg at $\Delta\beta$=*1* deg increments are performed at α=*10.48* and *14.67* deg. The corresponding correlation dataset from the DLR TN2545 wind tunnel test [22] are listed in the first column. All cases will be computed on the G1, G2, and G3 grids from Table 1. The Spalart-Allmaras (SA), Mentor Sheer Stress Transport (SST), and k-ε (KE) turbulence models will be assessed on select grids.

Table 3 - Static α/β-sweeps. SACCON DLR-F19.

DLR TN2545	*LOB/LIB* [°]	*ROB/RIB* [°]	α [°]	β [°]	M_∞	Re_{cref} [million]
1001	-	-	0-30	0	0.146	1.57
1103	-20/-20	+20/+20	0-30	0	0.146	1.57
1007	-	-	10.48	+10…-10	0.146	1.57
1109	-20/-20	+20/+20	10.48	+10…-10	0.134	1.46
1008	-	-	14.67	+10…-10	0.146	1.57
1110	-20/-20	+20/+20	14.67	+10…-10	0.134	1.46

B. DLR-F19: Forced oscillation in pitch

The AVT-201 common test cases for forced oscillation in PITCH are listed in Table 4. Two reduced frequencies for sinusoidal pitch oscillations (k_P=*0.06* and *0.12*) are assessed for $\Delta\Theta$=+/-4.7 deg about the nominal pitch angle Θ_0=10.3 deg, with and without control surface deflections. The corresponding correlation dataset from the DLR TN2545 wind tunnel test [23] are listed in the first column. The pitch oscillations were produced by a pitch link support with 6^0 crank angle and an axis push rod. Hence, there was relative motion between the SACCON and the post support sting that was not modeled in the computations. The Mach and Reynolds numbers are adjusted in the computations to correspond with their respective test conditions. The appropriate grids were selected from the results of the static study.

Table 4 - Common dynamic test cases for PITCH F-O. SACCON DLR-F19. $\Phi_0=0^o$, $\Psi_0=0^o$.

DLR TN2545	*LOB/LIB* [°]	*ROB/RIB* [°]	Θ_0 [°]	$\Delta\Theta$ [°]	f [Hz]	k_P $2\pi fc_{ref}/U_\infty$	M_∞	Re_{cref} [million]
2342-50	-	-	10.3	4.7	1	0.06	0.146	1.57
2351-59	-	-	10.3	4.7	2	0.12	0.146	1.57
2666-74	-20/-20	+20/+20	10.3	4.7	0.94	0.06	0.138	1.49
2675-83	-20/-20	+20/+20	10.3	4.7	1.88	0.12	0.138	1.49

C. DLR-F19: Forced oscillation in yaw

The AVT-201 common test cases for forced oscillation in YAW are listed in Table 5. Two reduced frequencies for yaw oscillation (k_Y=*0.10* and *0.19*) are assessed for $\Delta\Psi$=+/-5 deg sinusoidal oscillations at a pitch angle of Θ_0=10.1 deg, with and without control surface deflections. The run numbers from the corresponding correlation DLR TN2545 wind tunnel [23] dataset are listed in the first column. The Mach and Reynolds numbers

are adjusted in the computations to correspond to their respective test conditions. The appropriate grids were selected from the results of the static study.

Table 5 - Common dynamic test cases for YAW F-O. SACCON DLR-F19. $\Phi_0=0^o$, $\Psi_0=0^o$.

DLR TN2545	*LOB/LIB* [°]	*ROB/RIB* [°]	Θ_0 [°]	$\Delta\Psi$ [°]	f [Hz]	k_Y $2\pi\, fb_{ref}/U_\infty$	M_∞	Re_{cref} [million]
2270-78	-	-	10.1	5	1	0.10	0.146	1.57
2279-87	-	-	10.1	5	2	0.19	0.146	1.57
2162-70	-20/-20	+20/+20	10.1	5	0.94	0.10	0.138	1.49
2171-79	-20/-20	+20/+20	10.1	5	1.88	0.19	0.138	1.49

D. DLR-F17: Forced oscillation in roll

The ROLL oscillation cases for the AVT-161 DLR-F17 configuration are listed in Table 6. These consist of prescribing sinusoidal roll oscillations of $\Delta\Phi=\pm 5$ deg at 7 frequencies for $\Theta_0=10$ and 20 deg. The corresponding run numbers from the NASA dataset T134 [4] are listed in the first column. The T134 Mach and Reynolds numbers are $M_\infty=0.053$ and $Re_{cref}=0.375$ million.

Table 6- Dynamic test cases for ROLL F-O. SACCON DLR-F17. $\Phi_0=0^o$, $\Psi_0=0^o$.

NASA T134	Θ_0 [°]	$\Delta\Phi$ [°]	f [Hz]	k_R $2\pi\, fb_{ref}/U_\infty$
17	10, 20	5	0.24	0.063
18	10, 20	5	0.36	0.095
19	10, 20	5	0.44	0.116
20	10, 20	5	0.55	0.145
22	10, 20	5	0.66	0.174
25	10, 20	5	0.86	0.227
12	10, 20	5	1.00	0.264

VI. Results and Discussion

Correlations of computational and experimental results are presented to assess CFD predictive capabilities for the static and dynamic S&C characteristics of the SACCON configuration with and without control surface deflections. A cursory α-sweep is generated with the DLR-F19 to provide overlap with prior SACCON computational results in Ref. [6] and to assess longitudinal aerodynamics of the configuration with deflected control surfaces. Then a series of β-sweeps are performed to assess grid and turbulence model sensitivities, and to investigate static lateral/directional S&C characteristics. Finally, correlations are presented with forced sinusoidal motion imposed about the pitch, yaw, and roll axes. For all force and moment coefficients, the reference area is S_{ref}=0.77m^2, c_{ref}=0.479m, and $b_{ref}=b/2$=0.769m, *MRP*[x,y,z]=[0.600, 0, 0]m. The pitch and yaw oscillations are imposed at the *RRP*[x,y,z]=[0.855, 0, 0]m location, and the moments are transferred to the *MRP*. The support stings are not included in the force and moment integrations. As a reminder, the cases with undeflected control surfaces will be designated CS0, and the cases with deflected control surfaces LOB/LIB=-20/-20, ROB/RIB=+20/+20 deg as CS20. All moment coefficients are presented in the body axis system and are designated as C_{MX}, C_{MY}, and C_{MZ}, for roll, pitch, and yaw, respectively.

A. DLR-F19 static aerodynamics

1. α-sweep

A series of static time-accurate USM3D flow solutions were generated on the DLR-F19 for thirteen angles of attack between 0 and 30 degrees to explore the sensitivity of turbulence model on the medium grids G2.00 and G2.20 (see Tables 1 and 3). The SA and SST turbulence models were applied to both grids, and the k-ε model only to the G2.20 with control surface deflection CS20.

The CS0 cases utilized a prescribed characteristic time-step of $\Delta t^* = 0.02$ where physical $\Delta t = \Delta t^* \cdot c_{ref} / U_\infty$. Solutions were advanced in time for 2000 time-steps allowing the flow residual of the inner iterations to drop 2.5-orders of magnitude, which typically requires 5 to 6 inner iterations of the 2nd-order physical time-step scheme. This approach provided a total of 40 characteristic time steps for solution convergence, which was verified. The CS20 cases required a more aggressive strategy due to the additional complexity of asymmetric control surface deflection. Hence, a characteristic time-step of $\Delta t^* = 0.10$ was prescribed for 2000 time steps, increasing the total number of characteristic time steps to 200. Some test solutions were run on the CS0 case to confirm that the change in Δt^* has negligible impact on the converged solution, which was expected due to the strong flow damping from Reynolds averaging.

Comparisons of lift, drag, and pitching moment coefficient variations with angle of attack are presented in Fig. 8 for both CS0 (left) and CS20 (right) configurations. The flow physics behind the behavior of the experimental data [22] with increasing angle of attack, α, is well documented [11] and will not be repeated. The correlations of USM3D SA and SST turbulence model results for the undeflected CS0 case is similar to that published during AVT-161 [24]. In general, both the SA and SST correlate well for C_L and C_D in the linear range up to $\alpha \approx 15$ deg. The C_{MY} is under predicted in the linear range, which was typical of all RANS correlations from the AVT-161 task group [6-13]. A stronger sensitivity is observed at the higher post-stall angles. Note the large uncertainty bands on C_{MY} for the experimental data above $\alpha > 17$ deg, which infer highly unsteady flow. The poor correlations of CFD in this range suggest that the inherent dissipation of the RANS formulation caused by excessive levels of viscosity damps any critical unsteady flow features that would influence this sensitive region of the angle-of-attack range. The SST model does yield a better correlation of post stall due to its known quality of producing lower levels of turbulent viscosity than SA for highly separated flows.

The deflected CS20 correlations on the right of Fig. 8 reflect the general character of the CS0 case. However, in addition to the SA and SST models, the KE (k-ε) model has been added. The KE model offers no significant improvement to the correlations with experimental data. Furthermore, this model failed to run beyond $\alpha = 20$ deg, thereby preventing any assessment in the post-stall region.

2. β-sweeps

A series of static sideslip sweeps (Table 3) were generated on the DLR-F19 to explore the sensitivity of grids (Table 1) and turbulence models. The SA, SST, and KE turbulence models were applied to both CS0 and CS20 grids.

A physical time step $\Delta t = 0.00167$s was prescribed for the sideslip sweeps, which results in a characteristic time-step of $\Delta t^* = 0.165$. A total of 25 inner iterations were performed between each time step. The sweeps were computed with one continuous run using the prescribe motion capability from FDCADRE. Restarting from a converged zero-sideslip initial solution at angle of attack, the configuration was moved in 1 degree increments of sideslip over 10 time steps and then held on point for 290 time steps ($\Delta t^* \approx 48$) before moving to the next point. Convergence to steady state was confirmed within each increment. The advantages of this strategy are that it 1) requires a factor of 3.5 less computer time than a comparable set of individual runs, and 2) mimics the wind tunnel test technique, which could potentially have path dependencies that affect the progression of leading-edge flow separation with increasing sideslip.

The selection of the baseline grids for CS0 and CS20 is determined from the results in Fig. 9, which convey the variations of static roll, pitch, and yaw moments, C_{MX}, C_{MY}, and C_{MZ}, with β at the more challenging pitch angle $\Theta_0 = 14.67$ deg. The TN2545 experimental data [22] are plotted with symbols and uncertainty bounds. Note that the moments for the CS0 case on the left are relatively symmetric, whereas those for CS20 with asymmetric control deflections are less so. Solutions were computed with USM3D/SA on grids G1, G2, and G3 from Table 1. For the symmetric CS0 cases, solutions were only computed in the positive β-sweep direction (nose left). It is immediately obvious that G1 is not adequate for either CS0 or CS20 cases. Grids G2 and G3 generally capture the slope of the moments (i.e. static stability), and to a lesser extent the inflection in C_{MX} and C_{MZ} at $\beta \approx \pm 5$ deg caused by a sudden change in flow state. It is also encouraging that grids G2 and G3 also produce the correct offset in negative rolling moment $C_{MX} \approx -0.035$ at $\beta = 0$ deg for CS20. Differences are observed in the offset and character of C_{MZ} for CS20, but most of the USM3D/SA solutions fall within the uncertainty range of the data for C_{MX} and C_{MZ}. Considering the increasingly large cell count of grids G2 and G3, and their reasonably close correlation of results between these two grids in Fig. 9, the G2.00 (13 million cells) and G2.20 (18 million cells) grids will be selected for further assessment of turbulence models.

Fig. 10 shows the effect of the SA, KE, and SST turbulence models on the static lateral/directional moment coefficients at the lower pitch angle $\Theta_0 = 10.48$ deg using the medium grids G2. Again, the CS0 is on the left, and

CS20 on the right. The TN2545 experimental data, plotted with symbols and uncertainty bounds, exhibit a well behaved, almost linear quality. The USM3D solution results from the three turbulence models also correlate reasonably well with experiment. However, the SST model renders the best overall correlation.

A similar correlation of turbulence models for the higher pitch angle Θ_0=14.67 deg in Fig. 11 yields a more surprising result. The SST model degenerates dramatically for both CS0 and CS20 beyond β of ±2 degrees, whereas the SA and KE models retain reasonable correlations. The reason for this departure is evident in the corresponding surface C_p contours and streamlines presented in Fig. 12 for β=+5 deg. At this sideslip, the rolling moment C_{MX} in Fig. 11 for the SST solution on the CS0 case shows a sudden departure in the positive direction away from the TN2545 data and the SA/KE solutions. Similarly the yawing moment C_{MZ} for the CS20 solution with the SST model in Fig. 11 exhibits a similar sudden departure in the positive direction that extents well outside of the experimental uncertainty bounds. In Fig. 12, the SA and KE models produce a partially attached flow with accompanying low pressure along a majority of the right (windward) wing leading edge, and the beginnings of a leading-edge vortex near the left-wing tip. This is consistent with the production of a negative rolling moment C_{MX}. The SST model results in Fig. 12 reveal a well developed leading-edge vortex and accompanying low pressure on the left wing, and a more stalled flow with increasing pressures on the right wing, which is consistent with the production of a positive rolling moment C_{MX}. Numerous attempts were made to resolve the problem with the SST model, e.g. ran the finer G3 grids (Table 1), decreased time step Δt, increased number of inner iterations, decreased rate of incremental sideslip motion, initialized solution from free stream condition, etc., but nothing produced a significantly different result. In past experiences, the SST model has been a very reliable model of choice for many complex applications. However, it appears that the SACCON configuration at this higher angle of attack sideslip condition has exposed a shortcoming in the turbulence model.

Overall in Fig. 11, the KE model yields the best correlations with TN2545 data. Unfortunately, KE solutions could not be obtained for β<-6 deg. Hence, this model lacks the robustness for general use on the SACCON. For these reasons, the SA model is selected as the model of choice for SACCON S&C modeling, and will be utilized in the forced oscillation computations that follow.

B. Forced oscillation (F-O)

Sinusoidal oscillations about the pitch and yaw axes were imposed on the DLR-F19 SACCON at *RRP*[x,y,z]=[0.855, 0, 0]m through the FDCADRE trajectory input file. The roll oscillations for the DLR-F17 were prescribed by an internal motion generator within USM3D. The forced oscillation computations were initiated by solution restart from converged time-accurate static solutions at the nominal pitch angle Θ_0 (α_0), roll angle Φ_0=0, and yaw angle Ψ_0=0 deg. Although the dynamic force and moment coefficients are essentially converged to their periodic solution after the first quarter-oscillation cycle, the solutions are continued for two full sinusoidal cycles in this study. The second cycle is utilized for comparisons to eliminate any transients from the plots. The time-accurate RANS solution exhibits a deterministic quality by converging to a very stable solution, in contrast to the well known unsteadiness in the experimental data. The support sting moves with the wing in solid body motion, but is not included in the force and moment integrations. The moments are transferred from the RRP to the MRP.

The USM3D convergence guidelines for dynamic RANS simulations are developed in Ref. [6]. In general, a well-converged solution is insured using a total of 36,000 iterations per oscillation cycle, regardless of the combination of outer time steps and inner iterations. This guideline is overly conservative for many conditions, but does insure convergence of the more difficult nonlinear cases using a single strategy.

A physical time step of Δt=0.00167s was selected for the current computations to match that in the experimental data. For CS0 cases with oscillation frequencies of 1.00Hz and 2.00Hz, this results in a Δt^*=0.174 and respective time-steps per cycle of 600 and 300 with corresponding inner iterations of 60 and 120 to maintain a total of 36,000 total iterations per cycle. Similarly for CS20 cases with oscillation frequencies of 0.94Hz and 1.88Hz, the Δt^*=0.165 with respective time-steps per cycle of 638 and 320 with corresponding inner iterations of 56 and 113.

1. Pitch F-O of DLR-F19 SACCON

The cases for pitch oscillation of the DLR-F19 are listed in Table 4. Low and high frequency oscillations of $\Delta\Theta$=±4.7 deg about an initial pitch angle of Θ_0=10.3 deg are investigated for $k_P=2\pi f\, c_{ref}/U_\infty$ of 0.06 and 0.12. These reduced frequencies correspond respectively to 1.00Hz and 2.00Hz for CS0, and 0.94Hz and 1.88Hz for CS20 cases.

An important inconsistency in configuration was noted in Section II.B where the experimental TN2545 pitch oscillations [23] were imposed using a pitch link support with a 6^0 crank angle and an axis push rod. Hence, there was relative motion between the stationary post support sting and the oscillating SACCON configuration. For current computational results, the SACCON is supported by the 15^0 cranked yaw-link sting and pitch oscillations

were imposed as a solid body rotation of the entire grid, which contains no relative motions between the sting and wing.

The pitch oscillation correlations are shown for the low frequency (k_P=0.06) in Fig. 13, and high frequency (k_P=0.12) in Fig. 14. These figures portray the effect of grid density G1 and G2 using the USM3D/SA model on the aerodynamic response to the motion, which manifest as hysteresis loops for C_N, C_{MY}, and C_{MZ} that oscillate in pitch in the counter-clockwise direction between $5.6 \leq \alpha \leq 15$ deg. The effect of grid density is noticeable, but not large. The choice of turbulence model has a much greater impact as demonstrated in Ref. [24]. For computing dynamic stability derivatives, the shape of the hysteresis curves is the indicator of dynamic stability characteristics. In particular, the width of the hysteresis loop ΔC_M=(C_{M+} - C_{M-}) at α_0=10.3 deg is proportional to the dynamic damping coefficient [2]. Here, C_{M+} is the moment coefficient across α_0 with increasing angle, and C_{M-} is the moment coefficient across α_0 with decreasing angle. (The vertical offsets observed between experiment and CFD are related to the static offset that often occurs from turbulence model or grid effects; these have no bearing on the dynamic stability derivative.) For this case the ΔC_{MY} or ΔC_{MZ} at α_0=Θ_0=10.3 deg are presented in Table 7. Because of the counter-clockwise direction of pitch and yaw hysteresis, the increment in moments are negative which indicate damping. In general, the pitch damping from CFD tends to be slightly higher than experiment, but is still reasonably close. The yaw damping due to pitch oscillation is essentially negligible.

Table 7 – ΔC_{MY} and ΔC_{MZ} coefficients for DLR-F19 undergoing pitch oscillation at Θ_0=10.3^0

k_P	ΔC_M	CS0			CS20		
		TN2545	USM3D/SA		TN2545	USM3D/SA	
			G1.00	G2.00		G1.20	G2.20
0.06	ΔC_{MY}	-0.007	-0.0097	-0.0092	-0.0062	-0.0073	-0.0065
	ΔC_{MZ}	0.000	0.0000	0.0000	0.0002	-0.0004	-0.0004
0.12	ΔC_{MY}	-0.013	-0.0169	-0.0160	-0.012	-0.0143	-0.0123
	ΔC_{MZ}	0.000	0.0000	0.0000	0.0002	-0.0003	-0.0004

2. Yaw F-O of DLR-F19 SACCON

The cases for yaw oscillation of the DLR-F19 are listed in Table 5. Low and high frequency oscillations of $\Delta\Psi$=±5 deg about initial angles of Θ_0=10.1 and Ψ_0=0 deg are investigated for $k_Y=2\pi f b_{ref}/U_\infty$ of 0.10 and 0.19. These reduced frequencies correspond respectively to 1.00Hz and 2.00Hz for CS0, and 0.94Hz and 1.88Hz for CS20 cases. The SACCON configuration was supported by the 15^0 cranked yaw-link sting for both the wind tunnel [23] and CFD models with no relative motion between sting and wing during yaw oscillations.

The yaw oscillation correlations are shown for the low frequency (k_Y=0.10) in Fig. 15, and high frequency (k_Y=0.19) in Fig. 16. These figures portray the effect of grid density G1 and G2 using the USM3D/SA model on the aerodynamic response to the motion, which manifests as hysteresis loops for C_{MX}, C_{MY}, and C_{MZ} that oscillate in the clockwise direction between $-5 \leq \Psi \leq +5$ deg. As with the pitch oscillation, the effect of grid density for yaw F-O is observed to be nominal.

The width of the hysteresis loops ΔC_{MX} and ΔC_{MZ}, where ΔC_M=(C_{M+} - C_{M-}) at Ψ_0=0, are collected in Table 8. Here, C_{M+} is the respective moment coefficient across Ψ_0 with yaw angle increasing toward nose right, and C_{M-} is the moment coefficient across Ψ_0 with yaw angle decreasing toward nose left. The levels of ΔC_{MX} and ΔC_{MZ} are very small due to the absence of any vertical surfaces. While very small, the ΔC_{MX} does change sign from negative to positive between CS0 and CS20, indicating a tendency to lose roll damping. In general, the positive increments correspond to clockwise oscillation loops that represent propelling, and negative increments correspond to counter-clockwise loops that indicate damping. In general, the ΔC_M from CFD is approaching 3-times larger than experiment for the yaw F-O. While no specific reason has been discerned, this comparison is between two small numbers. Hence, in the absence of any vertical control surfaces and the small projected area of wing thickness these increments are highly sensitivity to the smallest perturbations. In contrast, the previous pitch and subsequent roll F-O results experience a strong forcing function from the interactions of larger aerodynamic surface projections with motion.

Table 8 – ΔC_{MX} and ΔC_{MZ} coefficients for DLR-F19 undergoing yaw oscillation at $\Theta_0=10.1^0$

k_Y	ΔC_M	CS0			CS20		
		TN2545	USM3D/SA		TN2545	USM3D/SA	
			G1.00	G2.00		G1.20	G2.20
0.10	ΔC_{MX}	0.000	-0.0007	-0.0007	0.000	0.0003	0.0005
	ΔC_{MZ}	0.0003	0.0008	0.0009	0.0003	0.0010	0.0011
0.19	ΔC_{MX}	0.000	-0.0010	-0.0010	0.000	0.0004	0.0008
	ΔC_{MZ}	0.000	0.0017	0.0018	0.0007	0.0019	0.0021

3. Roll F-O of DLR-F17 SACCON

The cases for roll oscillation of the DLR-F17 with aft sting are listed in Table 6. Solutions were computed for seven frequencies of roll oscillation between $\Delta\Phi=\pm5$ deg at angles of attack of $\alpha_0=10$ and 20 deg. The reduced frequencies $k_R=2\pi f b_{ref}/U_\infty$ ranged between 0.063 and 0.264 (f=0.24Hz to 1.00Hz). For sake of brevity, only three of these cases are presented in Figures 17 to 19 to document the roll F-O hysteresis behavior and degree of correlation with experiment in a manner consistent with previous pitch and yaw results. Reference [25] utilized these solutions to explore the creation of reduce-order models from CFD data using system identification techniques.

The plots of C_{MX}, C_{MZ}, and C_Y vs. $\Delta\Phi$ presented in Fig. 17, 18, and 19 correspond to k_R=0.063, 0.145, and 0.264 (f=0.24, 0.55, and 1.00Hz), respectively. The left column portrays the $\alpha_0=10$ deg results, and the right column $\alpha_0=20$ deg. For each frequency, dynamic damping is evidenced in roll and yaw from the counter-clockwise oscillation loops, and propelling (non-damping) for the side force as evidenced by clockwise loops. It should be mentioned that some vertical offsets present in the experimental data at zero roll angle, typically caused by small asymmetries in the model geometry and possible flow angularity, have been subtracted out [4] to facilitate more consistent comparisons of shape with the CFD predictions. The vertical offset is computed as the average of the two zero-axis crossing values. The T134 wind tunnel data in Fig. 17-19 also include variation bars denoting the standard deviation of flow unsteadiness.

The effect of the SA/SST turbulence models on the coarsest grid G1a from Table 2 is shown in Fig. 17, 18, and 19. In general for $\alpha_0=10$ deg the CFD oscillation loops are in close agreement with the relatively steady experimental data and the effect of turbulence model is small, but less so at $\alpha_0=20$ deg. Referring back to the static data in Fig. 8, $\alpha=10$ deg corresponds to a more well behaved pre-stall condition, whereas $\alpha=20$ deg falls within a very unsteady post-stall flow condition. Excellent correlations are exhibited Figures 17 to 19 at $\alpha=10$ deg for C_{MX} across the frequency range, correctly predicting the increase in roll damping with increasing roll frequency. While the trends with increasing frequency are reflected correctly for C_{MZ}, and C_Y at $\alpha_0=10$ deg, there is a slight over prediction of the dynamic effect. At $\alpha_0=20$ deg the experimental data displays significantly more unsteadiness. As might be expected, the CFD solutions produce a more varied correlation with the data. An impact of turbulence model can also be observed at $\alpha_0=20$ deg with the SA model being in closer agreement with the mean value of the experimental data than the SST model.

The effect of grids G1a/G2a/G3a from Table 2 using the SA turbulence model at $\alpha_0=20$ deg are investigated in Fig. 18 (right) for the mid-frequency case f=0.55Hz. While grid refinement does produce better correlations with the experimental data, the dominate effect comes from the SST turbulence model. An investigation of the impact of these CFD solution uncertainties on the creation of reduced order models constructed by system identification techniques is reported in Ref. [25]. There, two methods are presented, harmonic analysis and a two-step linear regression, for estimating mathematical models useful for stability and control analysis that can be applied to both CFD simulations and wind tunnel measurements. This approach offers a model structure that can accommodate unsteady aerodynamic behavior of the DLR-F17 and characterize model parameter uncertainty. Regression analysis of the CFD/SST simulated data resulted in a steady-flow damping parameter in statistical agreement with the wind tunnel and CFD/SA cases but not for the unsteady term. For the CFD/SST case, the unsteady term was statistically different and with a much larger uncertainty bound than either wind tunnel or CFD/SA cases. Time history comparisons in Ref. [25] confirmed the reduced-order model agreement between the wind tunnel and CFD/SA model but the CFD/SST case showed the added uncertainty due to turbulence model selection.

V. Concluding Remarks

The state of aerodynamic stability and control predictive capability of time-accurate RANS methodology has been investigated for a 53-degree swept UCAV configuration with control surface deflections. The vehicle aerodynamics is dominated by the complex non-linear physics of round leading-edge vortex flow separation. Correlations with wind tunnel data are made for static longitudinal/lateral sweeps, and at varying frequencies of prescribed roll/pitch/yaw sinusoidal motion for the vehicle operating with and without control surfaces. The ultimate purpose for these investigations is to provide data and insight to researchers who are developing techniques for augmenting flight simulation models from low-speed CFD predictions of aircraft traversing non-linear regions of a flight envelope.

These investigations included assessments of grid and turbulence model sensitivities with control surfaces deflected asymmetrically and undeflected. The effect of control surface deflection on the 3-axis moment coefficients were modeled with comparable accuracy to that with undeflected surfaces for angle-of-attack and sideslip sweeps. For the static sideslip cases, the SST turbulence model exhibited premature leading edge flow separation and was deemed not suitable for further investigation. The SA turbulence model was selected as the most consistent approach for the full range of the test matrix. The roll/pitch/yaw forced oscillation computations produced dynamic stability characteristics consistent with that from the experimental data.

Acknowledgments

The work reported herein is funded by the Vehicle Systems Safety Technologies (VSST) project under the NASA Aviation Safety Program. The author would also like to thank Mr. Ed Parlette of ViGYAN, Inc. for generating the computational grids. Also, thanks is offered for Dr. Greg Power and Mr. Chris Robinson at Arnold Engineering and Development Center, and Dr. Mohagna Pandya of NASA Langley Research Center for invaluable help with application of the FDCADRE framework. And finally, special thanks is extended to my fellow AVT-201 team members for their synergistic interactions, and in particular to the excellent experimentalists who conceived, designed, built, tested, and produced final data sets for the SACCON wind tunnel models.

References

[1] Cummings, R.M., Schütte, A., "Integrated Computational/Experimental Approach to Unmanned Combat Air Vehicle Stability and Control Estimation", *Journal of Aircraft*, Vol. 49, No. 6, November-December 2012, pp. 1542-1557.

[2] Cummings, R.M., Schütte, A., Hübner, A., "Overview of Stability and Control Estimation Methods from NATO STO Task Group AVT-201", AIAA Paper 2013-0968, January 2013.

[3] Thompson, J.R., Frink, N.T. Murphy, P.C., "Guidelines for Computing Longitudinal Dynamic Characteristics of a Subsonic Transport", AIAA-2010-4819, June 2010.

[4] Vicroy, D.D., Löser, T.D., Schütte, A., "Static and Forced-Oscillation Tests of a Generic Unmanned Combat Air Vehicle," *Journal of Aircraft*, Vol. 49, No. 6, November-December 2012, pp. 1558-1583.

[5] Roosenboom, E.W.M, Konrath, R., Schröder, A., Pallek, D., Otter, D., Morgand, S., Gilliot, A., Monnier, J.C., Le Roy, J.F., Geiler, C., Pruvost, J. "Stereoscopic Particle Image Velocimetry Flowfield Investigation of an Unmanned Combat Air Vehicle", *Journal of Aircraft*, Vol. 49, No. 6, November-December 2012, pp. 1584-1596.

[6] Frink, N., "Strategy for Dynamic CFD Simulation on SACCON Configuration," AIAA Paper 2010-4559, June 2010.

[7] Vallespin, D., Boelens, O., and Badcock, K., "SACCON CFD Simulations Using Structured Grid Approaches," AIAA Paper 2010- 4560, June 2010.

[8] Tormalm, M., and Schmidt, S., "Computational Study of Static And Dynamic Vortical Flow over the Delta Wing SACCON Configuration Using the FOI Flow Solver EDGE," AIAA Paper 2010-4561, June 2010.

[9] Le Roy, J., "SACCON CFD Static and Dynamic Derivatives Using elsA," AIAA Paper 2010-4562, June 2010.

[10] Chakravarthy, S., and Chi, D., "SACCON CFD Simulations Using CFD ++," AIAA Paper 2010-4563, June 2010.

[11] Schütte, A., Hummel, D., and Hitzel, S., "Flow Physics Analysis of a Generic Unmanned Combat Aerial Vehicle Configuration", *Journal of Aircraft*, Vol. 49, No. 6, 2012, pp. 1638-1651.

[12] Cummings, R., Petterson, K., Jirasek, A., and Schmidt, S., "SACCON Static and Dynamic Motion Flow Physics Simulations Using COBALT," AIAA Paper 2010-4691, June 2010.

[13] Gortz, S., McDaniel, D.R., and Morton, S.A., "Towards and Efficient Aircraft Stability and Control Analysis Capability using High-Fidelity CFD," AIAA Paper 2007-1053, January 2007.
[14] Ghoreyshi, M., Jirásek, A., and Cummings, R.M., "Computational Investigation into the Use of Response Functions for Aerodynamic-Load Modeling", *AIAA Journal*, Vol. 50, No. 6, June 2012, pp. 1314-1327.
[15] Cummings, R.M., and Schütte, A., "The NATO STO Task Group AVT-201 on 'Extended Assessment of Stability and Control Prediction Methods for NATO Air Vehicles," 32nd AIAA Applied Aerodynamics Conference, AIAA, Atlanta, GA (submitted for publication).
[16] Frink, N. T., Pirzadeh, S. Z., Parikh, P. C., Pandya, M. J., and Bhat, M. K., "The NASA tetrahedral unstructured software system (TetrUSS)," *The Aeronautical Journal*, Vol. 104, No. 1040, 2000, pp. 491-499.
[17] Pirzadeh, S.Z., "Three-Dimensional Unstructured Viscous Grids by the Advancing Layer Method", AIAA Journal, Vol. 33, No. 1, 1996, pp. 43-49.
[18] Pirzadeh, S.Z., "Advanced Unstructured Grid Generation for Complex Aerodynamic Applications", AIAA Journal, Vol. 48, No. 5, 2010, pp. 904-915.
[19] Frink, N.T., "Tetrahedral Unstructured Navier-Stokes Method for Turbulent Flows", AIAA Journal, Vol. 36, No. 11, 1998, pp. 1975-1982.
[20] Pandya, M. J., Frink, N. T., Abdol-Hamid, K. S., Samareh, J. A., Parlette, E. B., and Taft, J. R., "Enhancements to TetrUSS for NASA Constellation Program," *Journal of Spacecraft and Rockets*, Vol. 49, No. 4, 2012, pp. 617-631.
[21] Power, G.D. and Calahan, J.A., "A Flexible System for Analysis of Bodies in Relative Motion", AIAA Paper 2005-5120, June 2005.
[22] Huber, K.C., Vicroy, D.D., Schütte, A., and Hübner, A., "UCAV Model Design and Static Experimental Investigations to Estimate Control Device Effectiveness and S&C Capabilities," 32nd AIAA Applied Aerodynamics Conference, AIAA, Atlanta, GA (submitted for publication).
[23] Vicroy, D.D., Huber, K.C., Loeser, T.D., and Rohlf, D., "Low-speed Dynamic Wind Tunnel Test Analysis of a Generic 53° Swept UCAV Configuration," 32nd AIAA Applied Aerodynamics Conference, AIAA, Atlanta, GA (submitted for publication).
[24] Frink, N.T., Tormalm, M. and Schmidt, S., "Three Unstructured Computational Fluid Dynamics Studies on Generic Uninhabited Combat Air Vehicle", *Journal of Aircraft*, Vol. 49, No. 6, 2012, pp. 1619-1637.
[25] Murphy, P.C., Klein, V., Frink, N.T., and Vicroy, D.D., "System Identification Applied to Dynamic CFD Simulation and Wind Tunnel Data", AIAA Paper 2011-6522, August 2011.

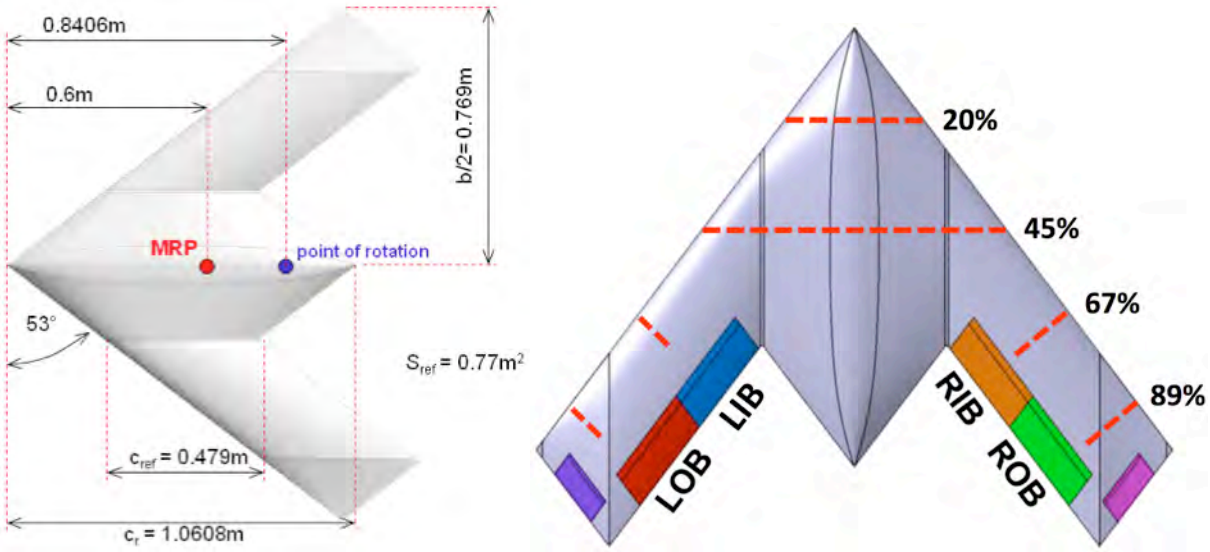

Figure 1. SACCON planform and geometric parameters, controls surface designations, and location of surface pressure orifices (red dashed lines).

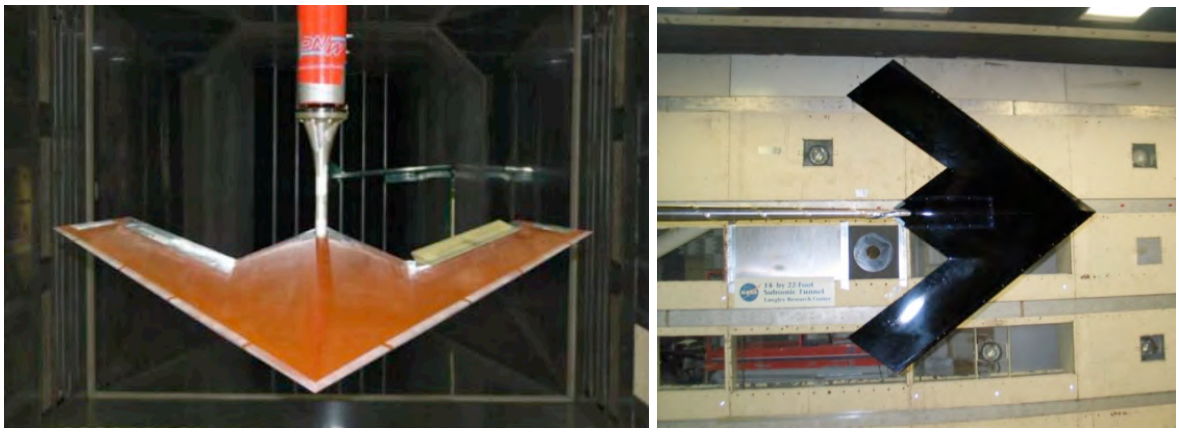

Figure 2. DLR-F19 with deflected control surfaces mounted on 15^{O} yaw-link in DNW-NWB tunnel (left). DLR-F17 mounted on aft-roll sting in NASA LaRC 14X22-Foot subsonic tunnel (right).

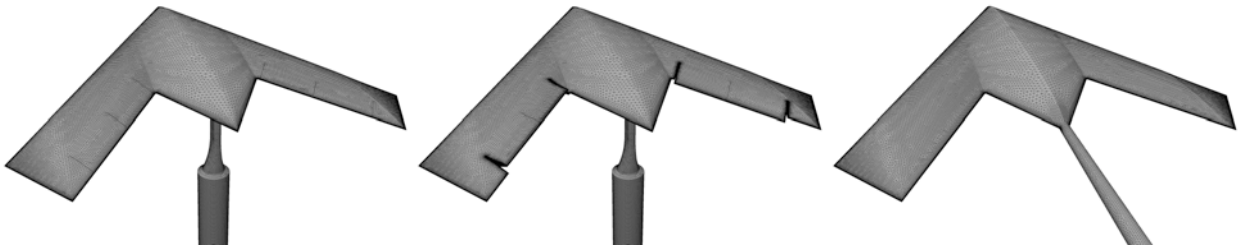

Figure 3. Grid 2 surface triangulations for DLR-F19 with CS0 and CS20, and DLR-F17 with aft sting. Left to right: G2.00, G2.20, G2a.

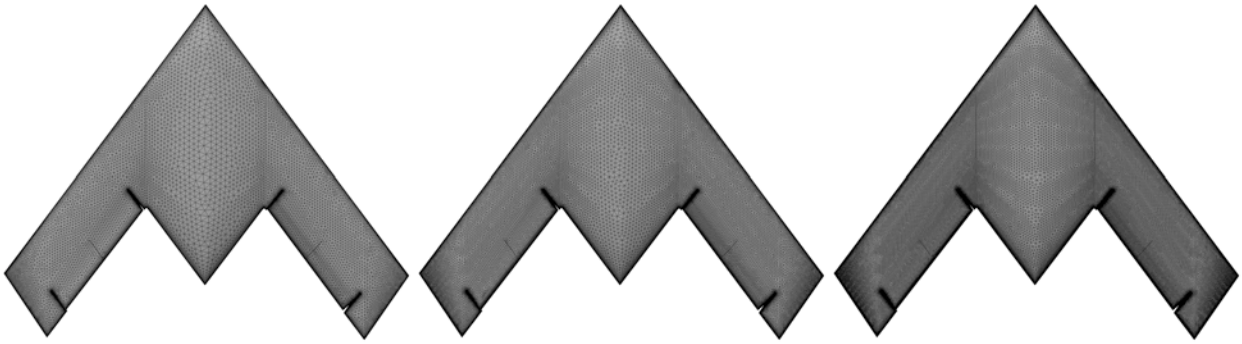

Figure 4. Upper surface triangulations for DLR-F19 CS20. Left to right: G1.20, G2.20, G3.30.

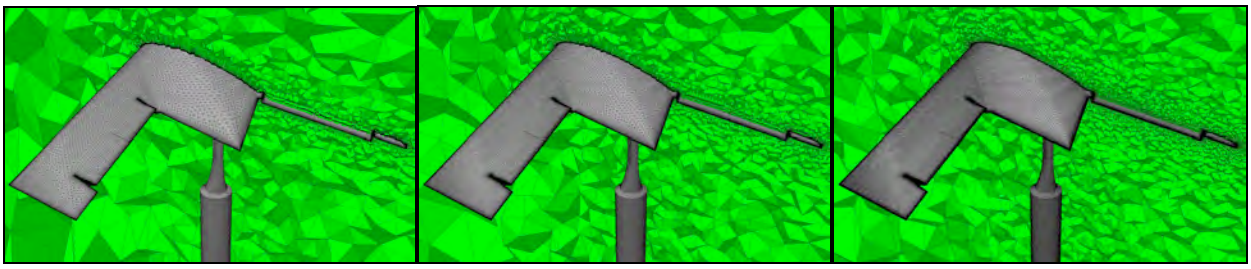

Figure 5. Volume grid through right-wing control surface of DLR-F19 CS20. Left to right: G1.20, G2.20, G3.30.

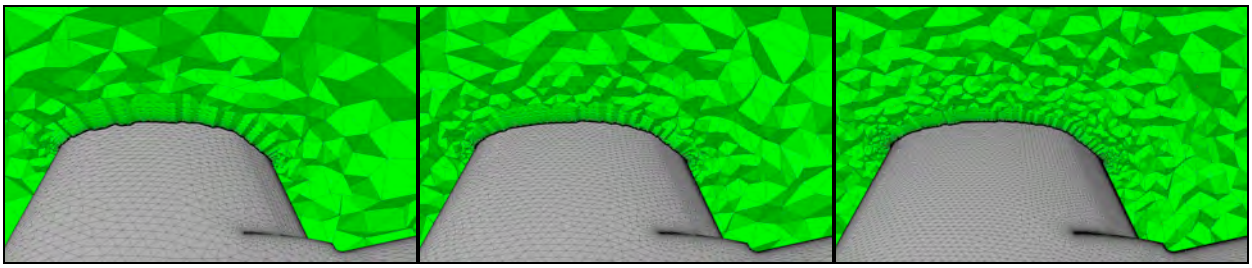

Figure 6. Volume grid slices perpendicular to leading edge through right-wing and deflected control surface for DLR-F19 CS20. Left to right: G1.20, G2.20, G3.20.

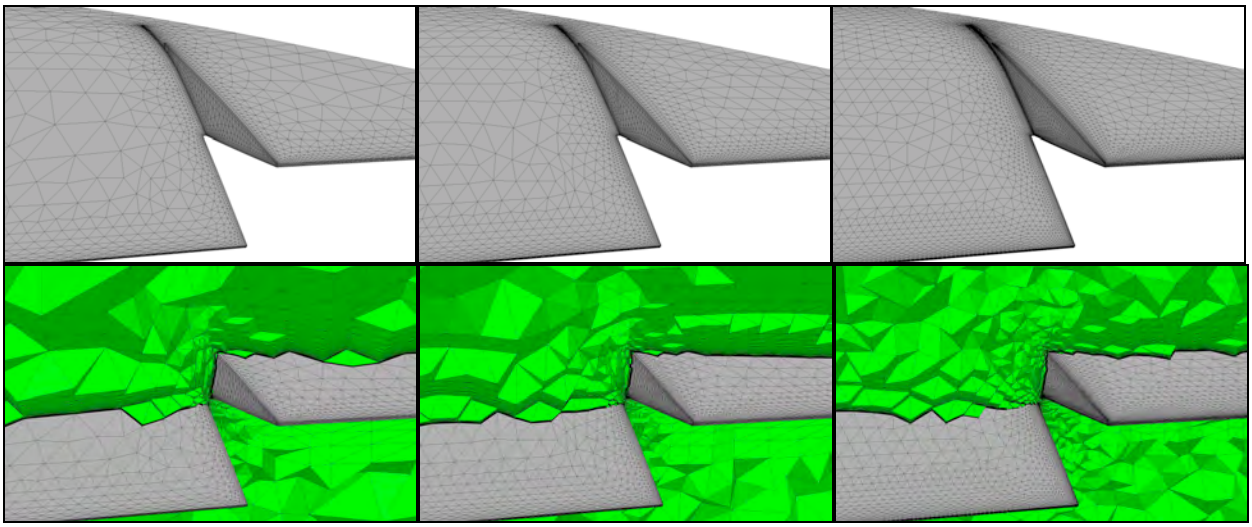

Figure 7. Close-up of right wing outboard flap gap for DLR-F19 CS20. Top: surface triangulation. Bottom: volume grid cut through control surface. Left to right: G1.20, G2.20, G3.20.

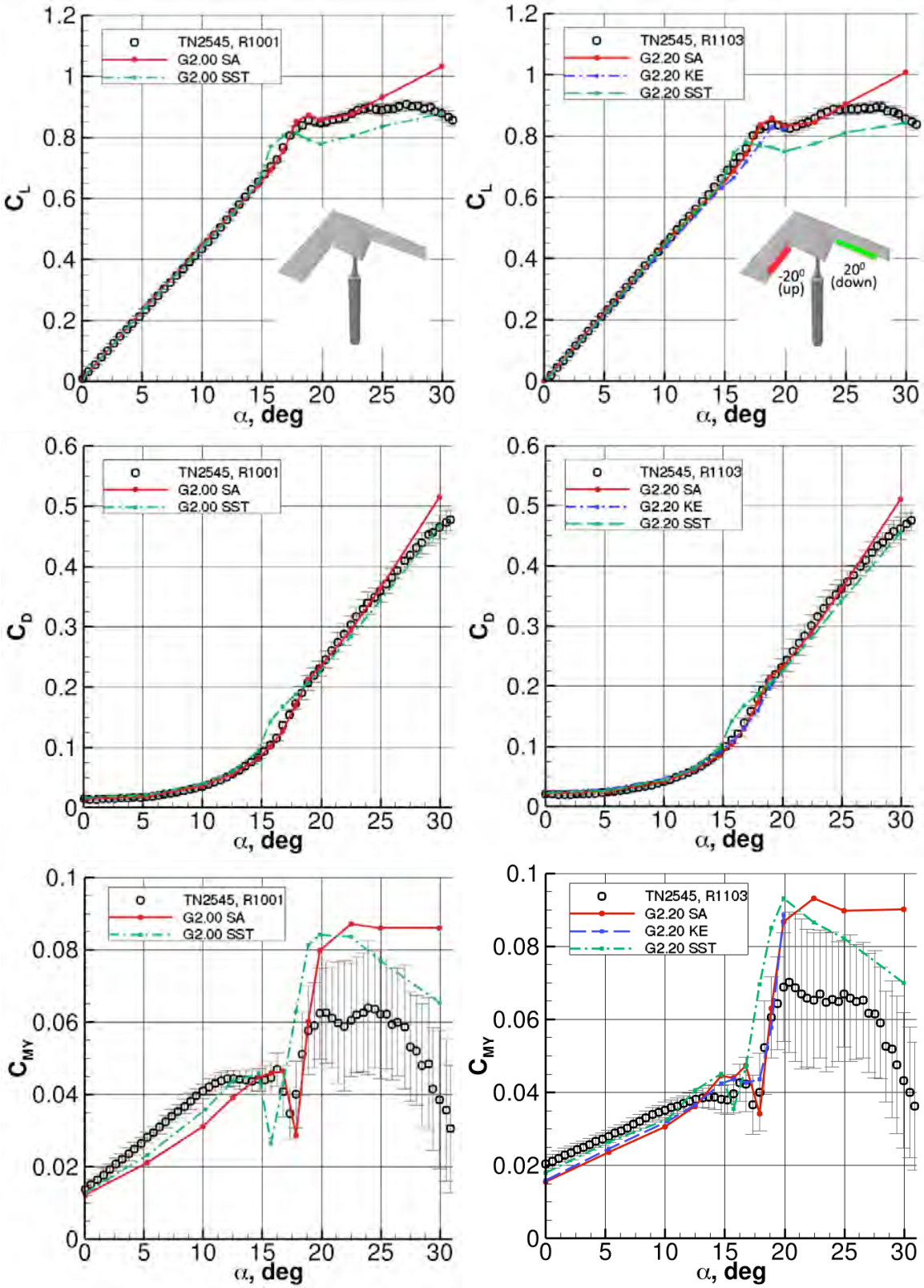

Figure 8. Effect of turbulence models on DLR-F19 for static lift, drag, and pitching moment coefficient. CS0 (left) and CS20 (right). M_∞=0.14, Re_{cref}=1.40 million. NASA USM3D, Grid 2.

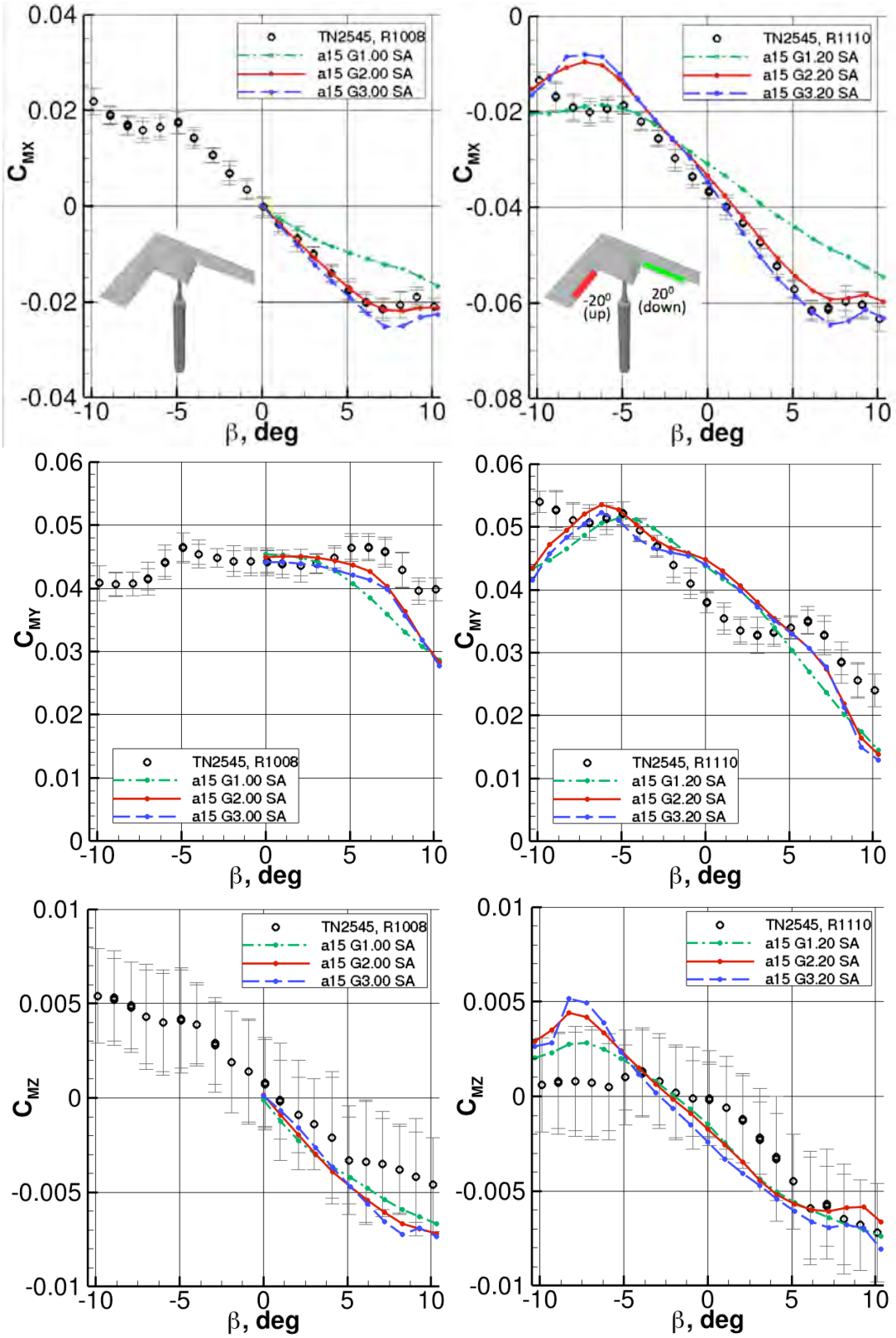

Figure 9. Effect of grid refinement on DLR-F19 static lateral/directional moment coefficients. CS0 (left) and CS20 (right). M_∞=0.14, Re_{cref}=1.40 million, Θ_0=14.67 deg. NASA USM3D/SA.

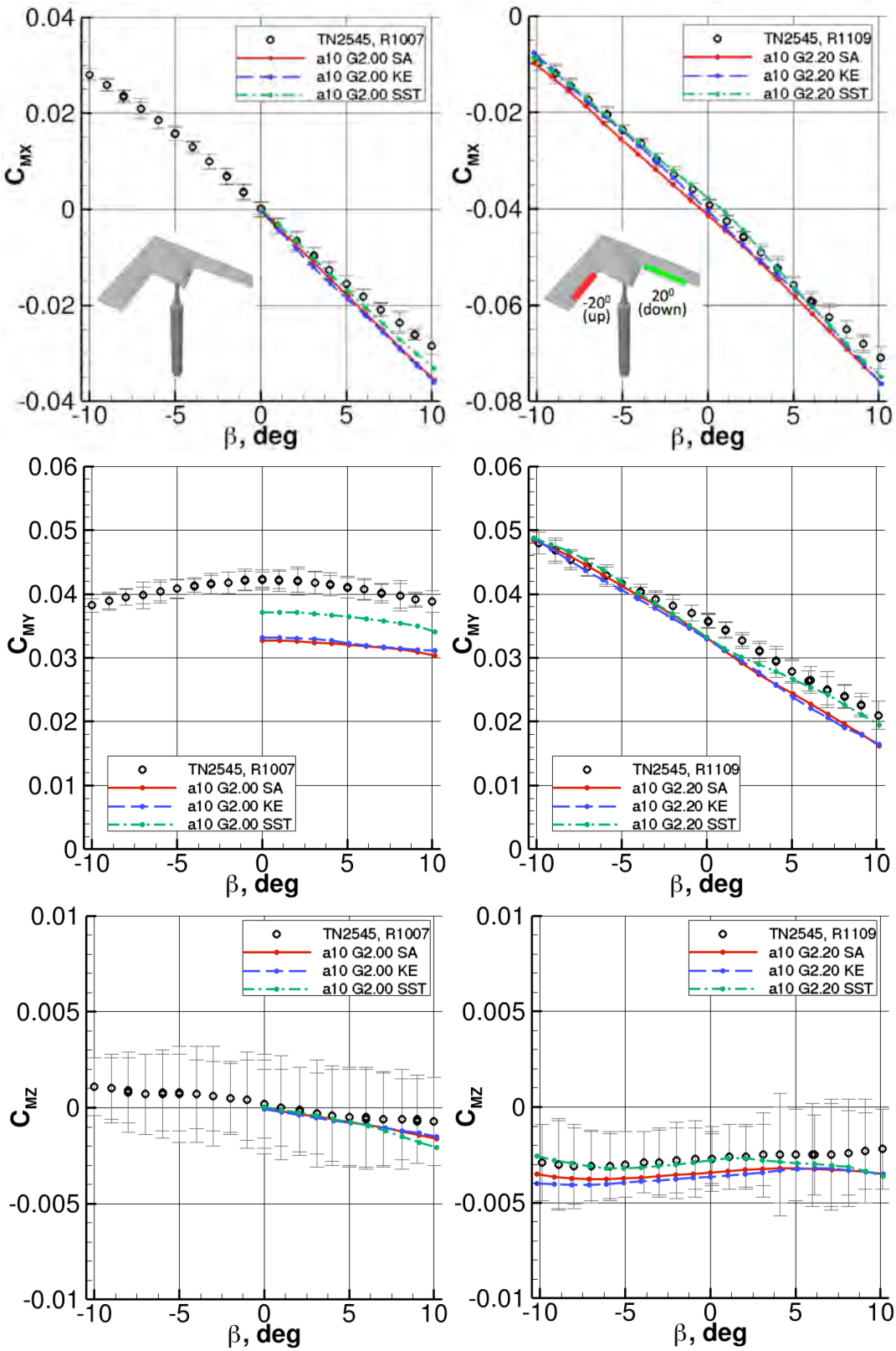

Figure 10. Effect of turbulence model on DLR-F19 static lateral/directional moment coefficients. CS0 (left) and CS20 (right). M_∞=0.14, Re_{cref}=1.40 million, Θ_0=10.48 deg. NASA USM3D, Grid 2.

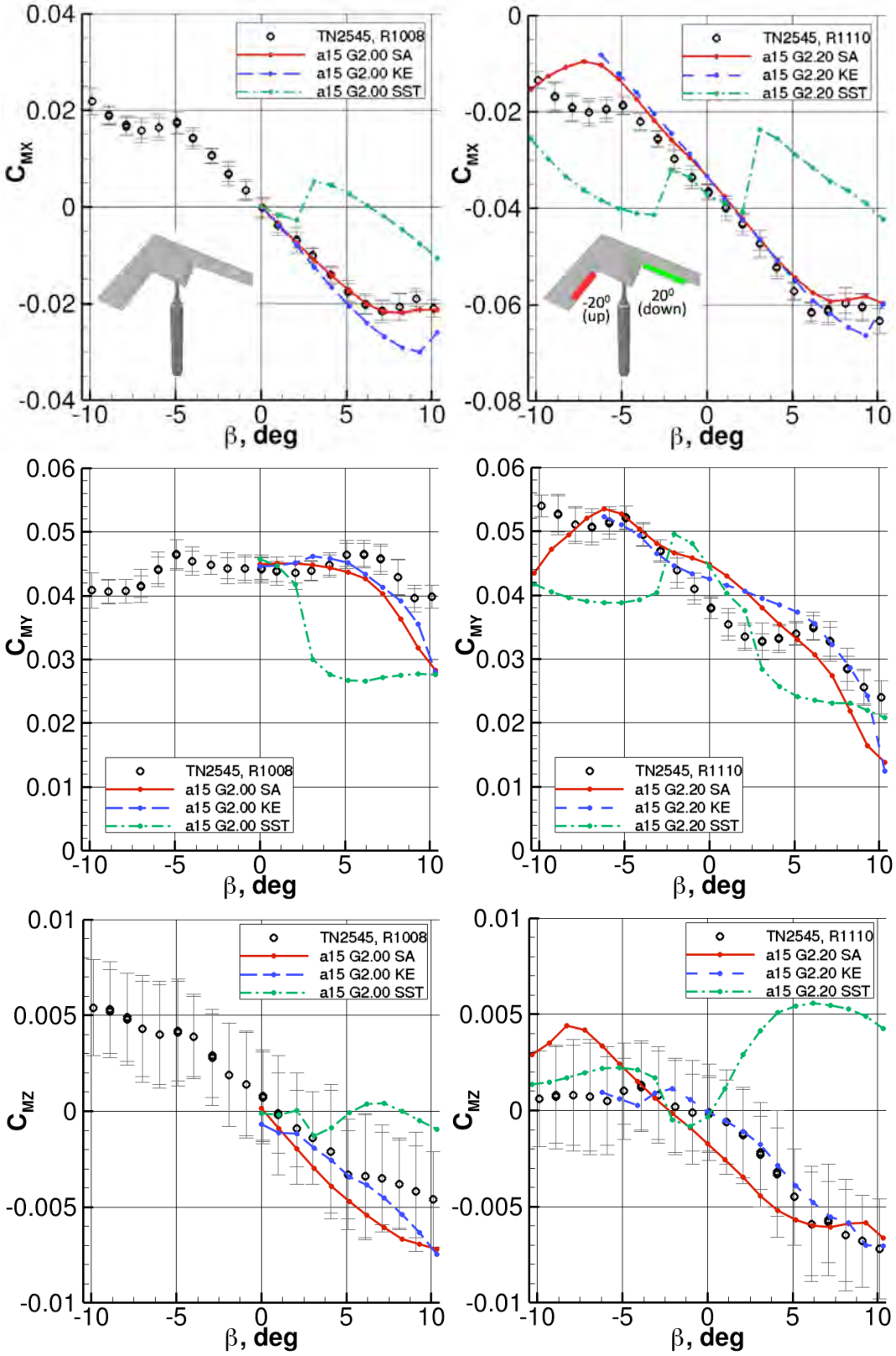

Figure 11. Effect of turbulence model on DLR-F19 static lateral/directional moment coefficients. CS0 (left) and CS20 (right). M_∞=0.14, Re_{cref}=1.40 million, Θ_0=14.67 deg. NASA USM3D, Grid 2.

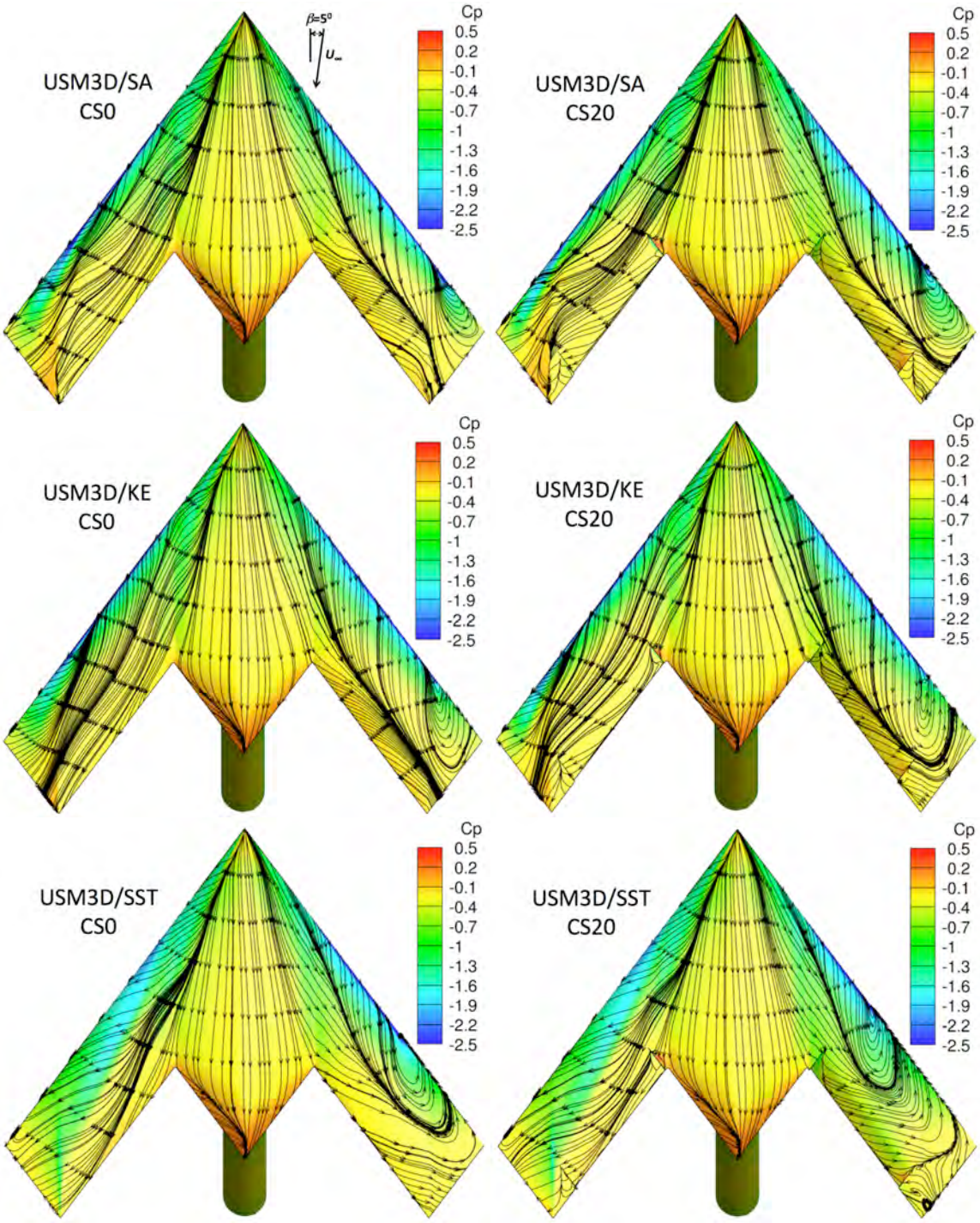

Figure 12. Effect of turbulence model on DLR-F19 surface C_p contours and streamlines at β=+5 deg. CS0 (left) and CS20 (right). M_∞=0.14, Re_{cref}=1.40 million, Θ_0=14.67 deg. NASA USM3D, Grid 2.

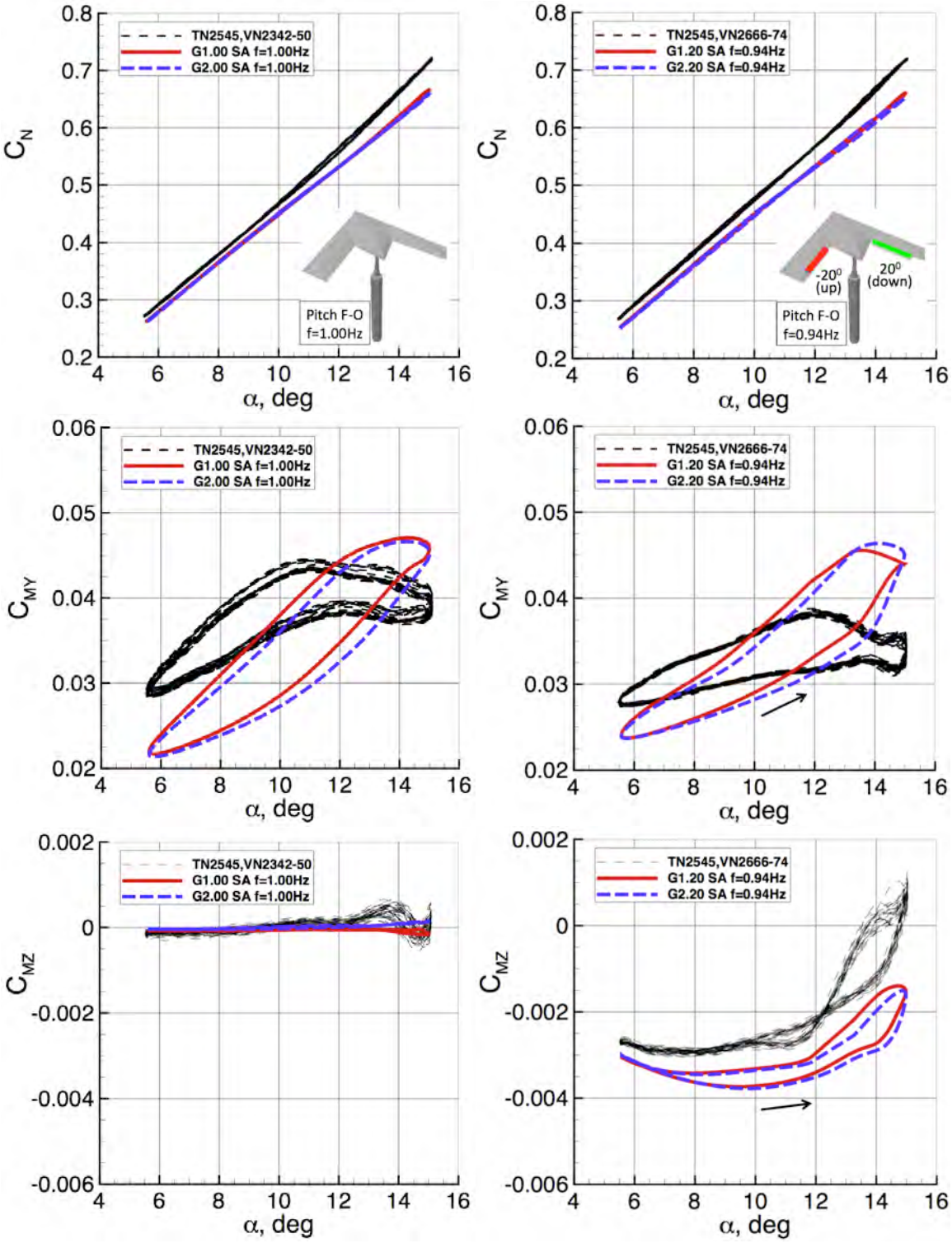

Figure 13. Effect of grid density on DLR-F19 longitudinal and directional coefficients under low frequency forced PITCH oscillation (k_P=0.06), Θ_0=10.3 deg, $\Delta\Theta$=±4.7 deg. CS0 (left) and CS20 (right). M_∞=0.14, Re_{cref}=1.5 million. NASA USM3D/SA, Grids 1 and 2.

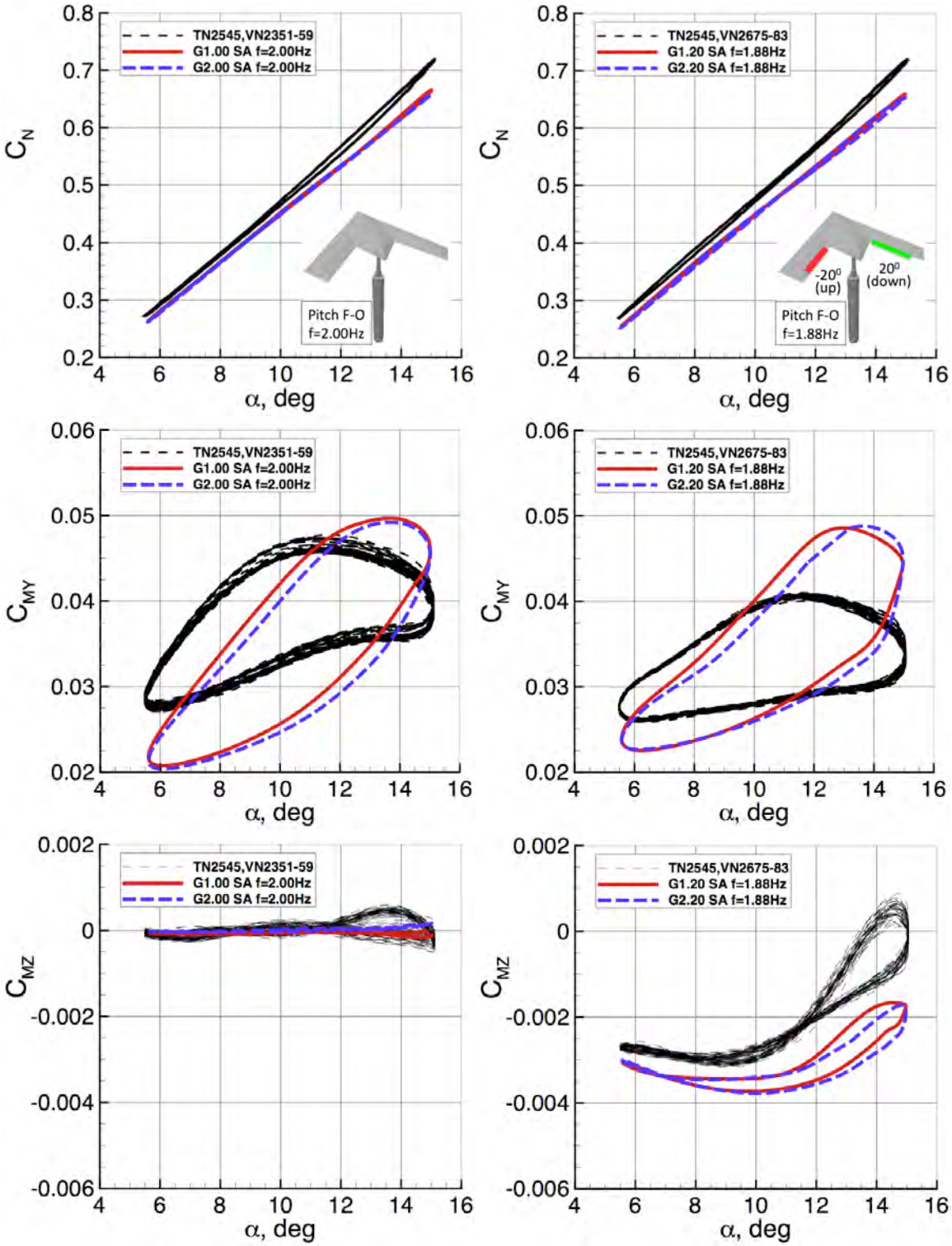

Figure 14. Effect of grid density on DLR-F19 longitudinal and directional coefficients under high frequency forced PITCH oscillation (k_P=0.12), Θ_0=10.3 deg, $\Delta\Theta$=±4.7 deg. CS0 (left) and CS20 (right). M_∞=0.14, Re_{cref}=1.5 million. NASA USM3D/SA, Grids 1 and 2.

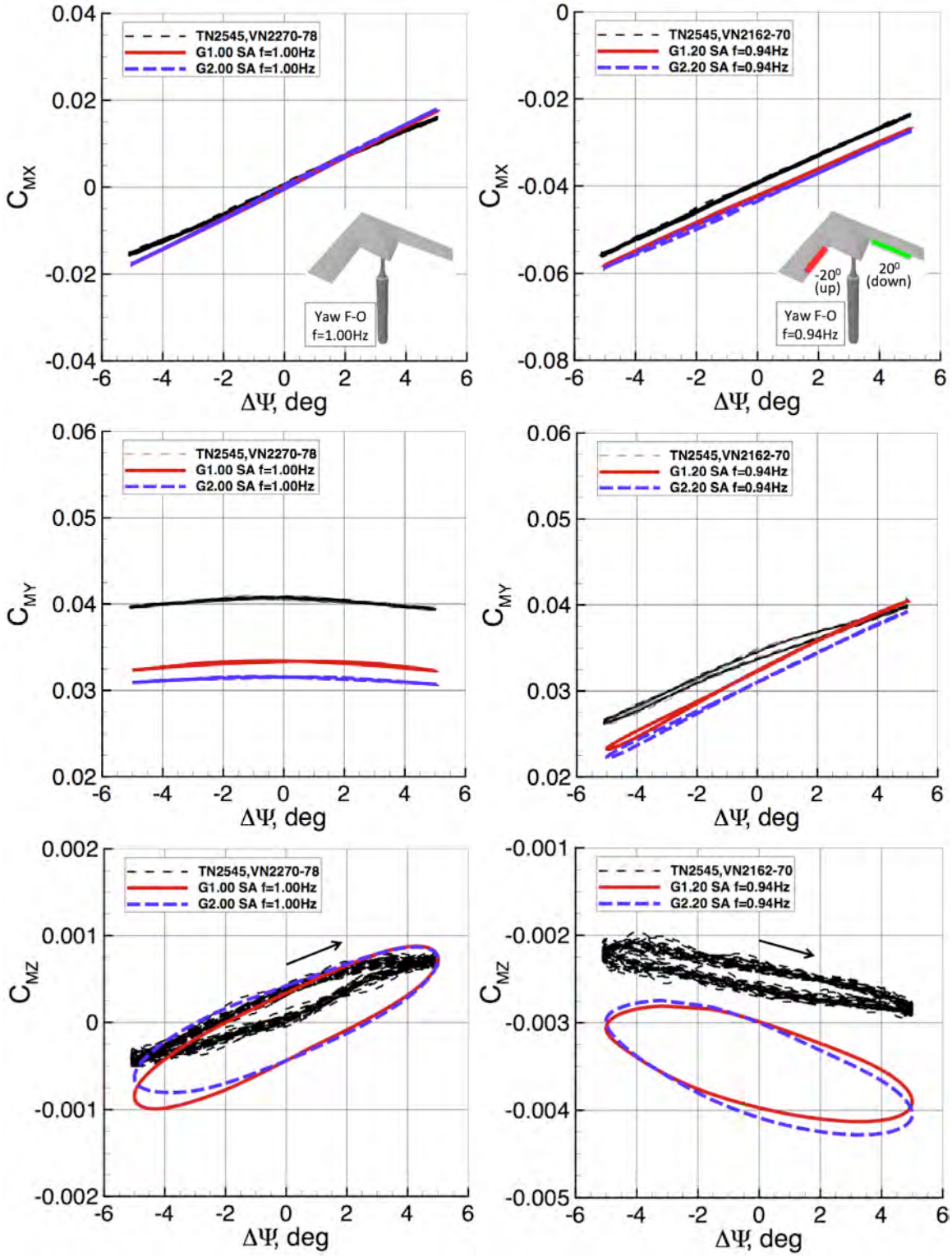

Figure 15. Effect of grid density on DLR-F19 lateral/directional moment coefficients under low frequency forced YAW oscillation (k_Y=0.10), Θ_0=10.1 deg, $\Delta\Psi$=±5.0 deg. CS0 (left) and CS20 (right). M_∞=0.14, Re_{cref}=1.5 million. NASA USM3D/SA, Grids 1 and 2.

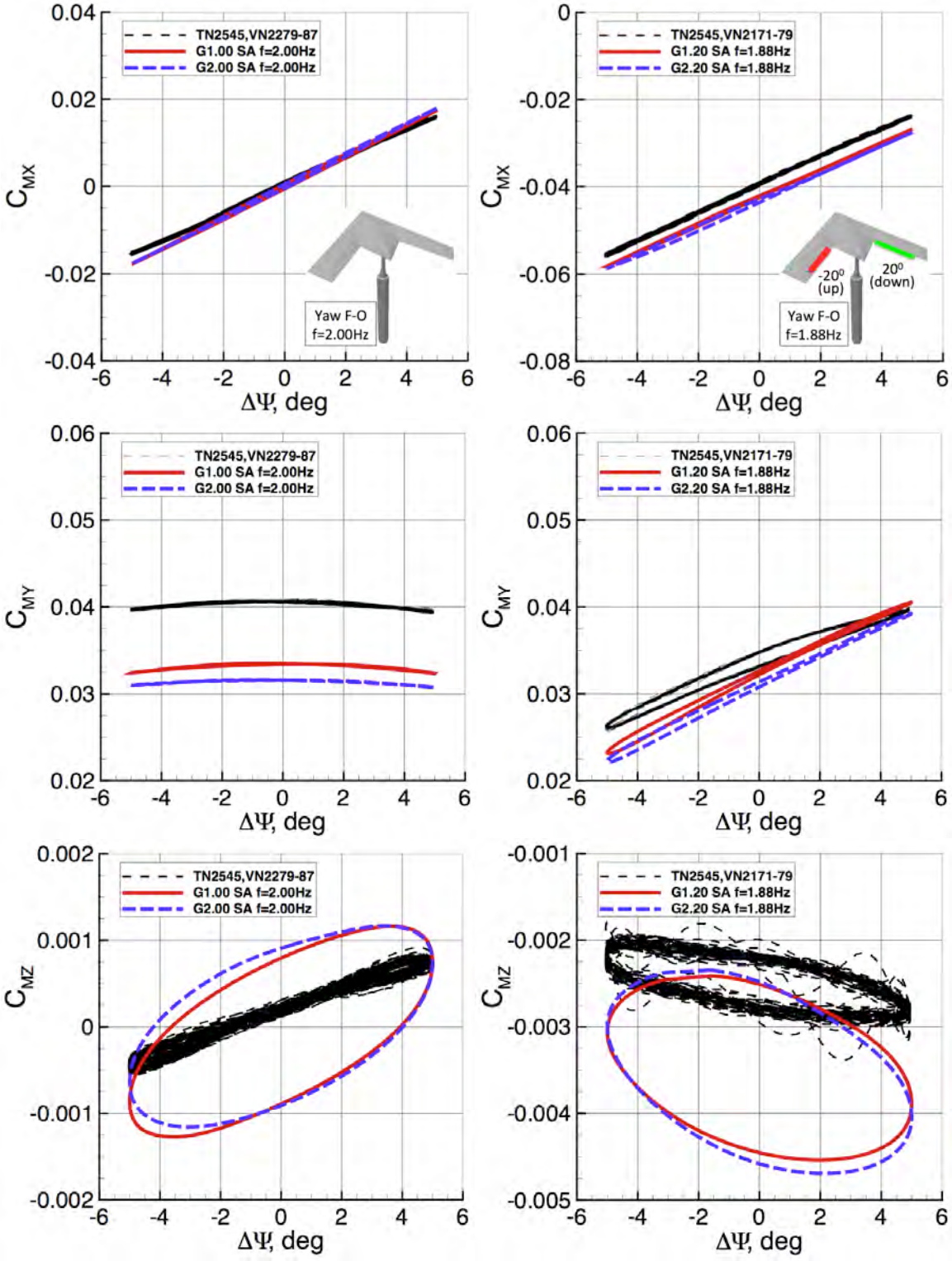

Figure 16. Effect of grid density on DLR-F19 lateral/directional moment coefficients under high frequency forced YAW oscillation (k_Y=0.19), Θ_0=10.1 deg, ΔΨ=±5.0 deg. CS0 (left) and CS20 (right). M_∞=0.14, Re_{cref}=1.5 million. NASA USM3D/SA, Grids 1 and 2.

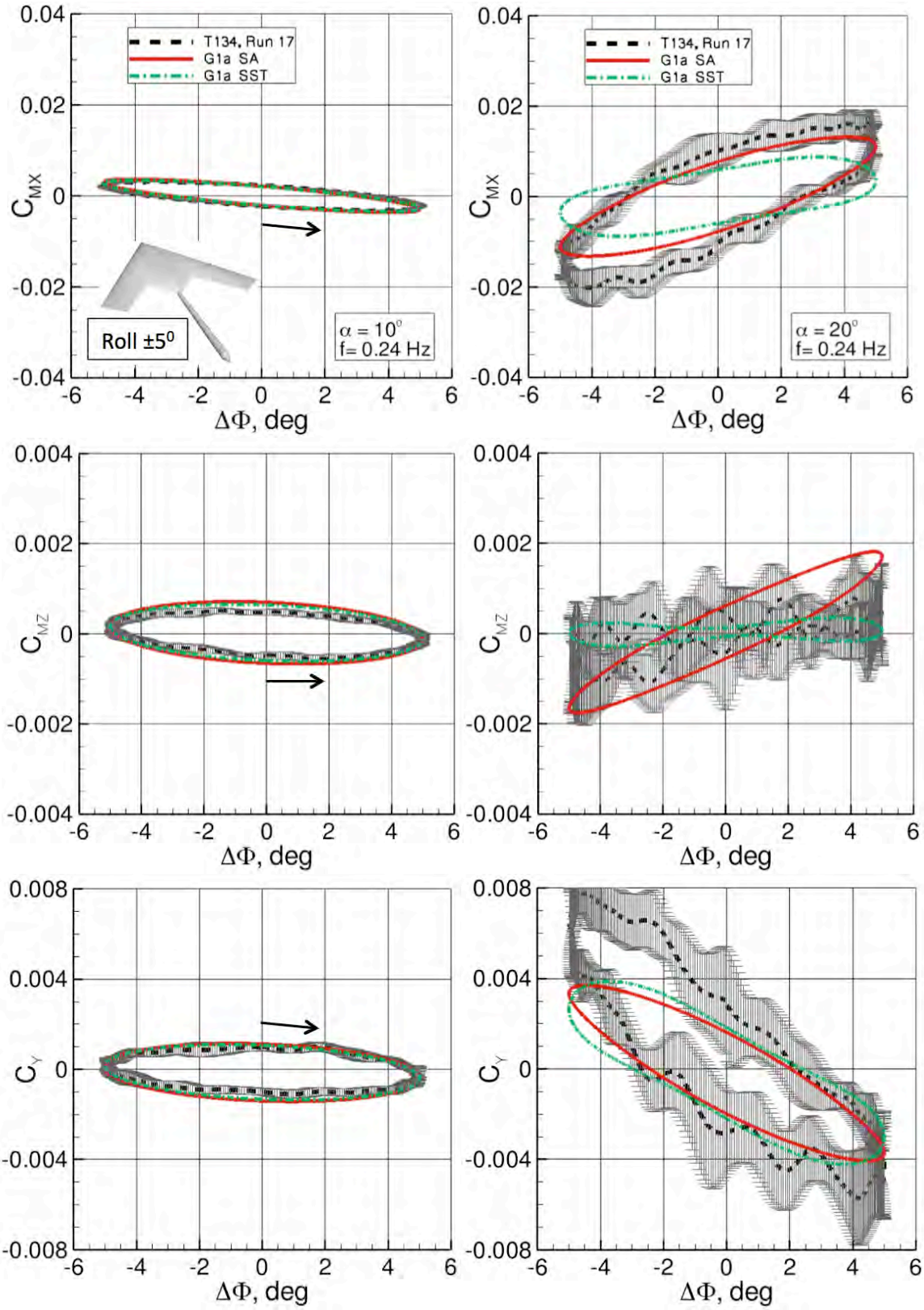

Figure 17. Effect of turbulence model on DLR-F17 lateral/directional coefficients under forced ROLL oscillation f=0.24Hz, k_R=0.063, ΔΦ=±5 deg. α=10 deg (left) and α=20 deg (right). M_∞=0.14, Re_{cref}=1.40 million. NASA USM3D/SA/SST, Grid 1a.

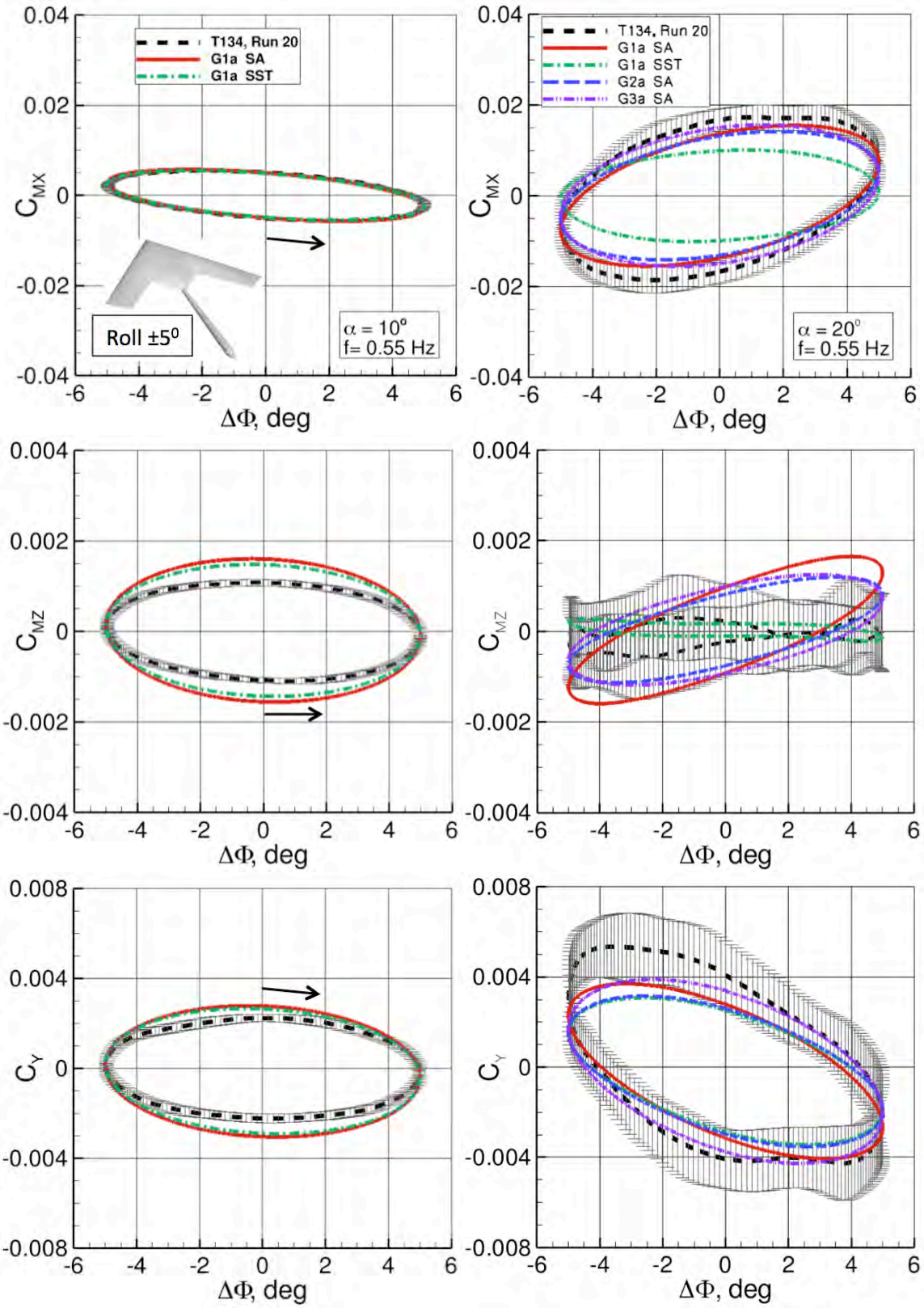

Figure 18. Effect of grid and turbulence model on DLR-F17 lateral/directional coefficients under forced ROLL oscillation f=0.55Hz, k_R=0.145, $\Delta\Phi$=±5 deg. α=10 deg (left) and α=20 deg (right). M_∞=0.14, Re_{cref}=1.40 million. NASA USM3D/SA/SST, Grids 1a and 2a.

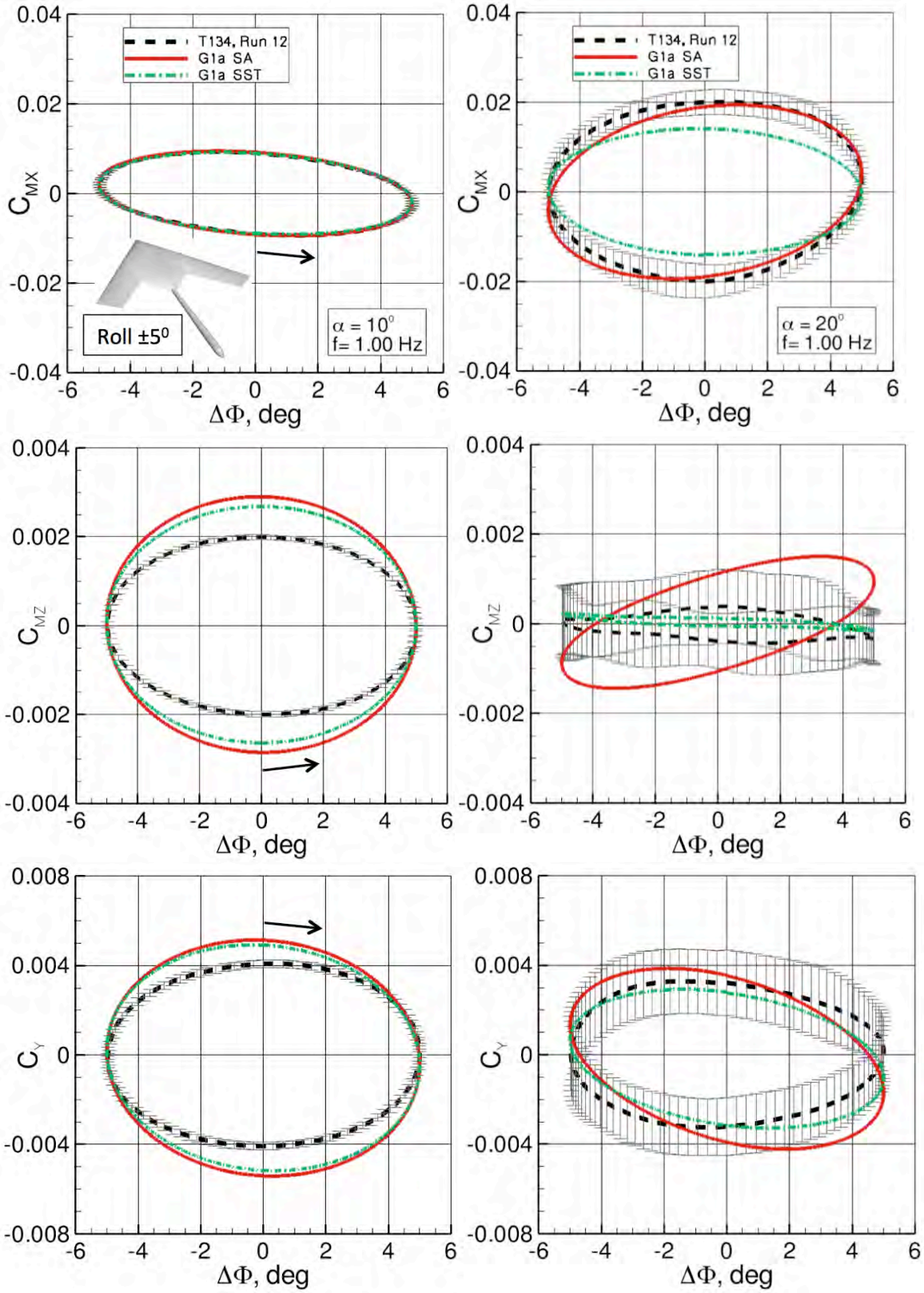

Figure 19. Effect of turbulence model on DLR-F17 lateral/directional coefficients under forced ROLL oscillation f=1.00Hz, k_R=0.264, ΔΦ=±5 deg. α=10 deg (left) and α=20 deg (right). M_∞=0.14, Re_{cref}=1.40 million. NASA USM3D/SA/SST, Grid 1a.